



Contents lists available at ScienceDirect

Arabian Journal of Chemistry

journal homepage: www.sciencedirect.com



Original article

Cell Lysis, labeling efficacy and biodistribution of intravenously administered Technetium-99 m labeled multifunctional zirconia nanoparticles in animal model

Ifra SanaUllah^a, Saira Riaz^{a,*}, Irfan Ullah Khan^b, Daoud Ali^c, S. Shamaila^d, M. Akram Raza^a, Amna Sajjad^e, Anjum N. Sabri^f, Shahzad Naseem^{a,*}^a Centre of Excellence in Solid State Physics, University of the Punjab, QAC, Lahore 54590, Pakistan^b Department of Cyclotron and Allied Radiopharmaceutics, INMOL Cancer Hospital, Lahore 54600, Pakistan^c Department of Zoology, College of Science, King Saud University, Riyadh 11451, Saudia Arabia^d Waterloo Institute for Nanotechnology, University of Waterloo, Ontario, Canada^e Department of Zoology, Government College University, Faisalabad, Pakistan^f Department of Microbiology and Molecular Genetics, University of the Punjab, QAC, Lahore 54590, Pakistan

ARTICLE INFO

Article history:

Received 23 May 2023

Accepted 12 September 2023

Available online 16 September 2023

Keywords:

Iron oxide
Zirconia
Honey
Anticancer
Drug loading

ABSTRACT

Nanoparticles, to be used in biomedical applications, have been the subject of extensive investigation in recent years. Recently, zirconia and iron have gained significant relevance to the field due to their superior mechanical and structural qualities as well as their numerous biological applications. In this research, Fe₃O₄-stabilized zirconia nanopowders are fabricated using a low-cost sol-gel approach. Iron oxide sol is added in 1–10 wt% increments to a 0.1 M zirconia sol. The obtained crystallite size values match well with previously reported values for the tetragonally stable (t-zirconia) phase. Hardness values of approximately 1278 HV, along with fracture toughness values of ~ 24.48 MPa.m^{-1/2} are observed for stable tetragonal zirconia. Results from cell lysis experiments indicate that the synthesized nanoparticles have the potential to combat cancerous cells. An encapsulation efficacy of up to ~ 73% is observed after a 120-minute time period. Radio labeling techniques are employed to label the as-synthesized zirconia nanoparticles using Sodium Pertechnetate (Na^{99m}TcO₄) labeled radiopharmaceuticals, allowing for biodistribution assessment. Multiple CT scans of rabbits are performed to obtain accurate results and evaluate their survival. Studies show that radiolabeled nanoparticles are highly absorbed in the animals' bladders, making them a promising choice for tumor therapy. Various physical properties of the animals are periodically examined after administration of the nanoparticle-based injection for several months, and no abnormalities are found. The results obtained through these characterizations indicate that these nanoparticles can be used as future therapeutic agents as well as drug carriers.

© 2023 The Author(s). Published by Elsevier B.V. on behalf of King Saud University. This is an open access article under the CC BY-NC-ND license (<http://creativecommons.org/licenses/by-nc-nd/4.0/>).

Abbreviations: CT scan, computerized tomography scan; Wt. %, Weight percent; NPS, nanoparticles; PVA, Poly vinyl alcohol; IOZH, Honey mediated Fe₃O₄-stabilized zirconia; DPPH, 2, 2, diphenyl-1-picrylhydrazyl; MTT, (3-(4, 5 dimethylthiazol-2-yl)-2, 5diphenyl tetrazolium bromide); SBF, Simulated body fluid; DMEM, Dulbecco's Modified Eagle's Medium; FBS, fetal bovine serum.

* Corresponding authors.

E-mail addresses: saira.cssp@pu.edu.pk (S. Riaz), shahzad.cssp@pu.edu.pk (S. Naseem).

Peer review under responsibility of King Saud University.



Production and hosting by Elsevier

1. Introduction

The pharmacological properties of a therapeutic agent are inherent and cannot be altered without various fractions of drugs. Due to their small size, nanoparticles serve as an excellent choice for blood transportation. Nanoparticles can be utilized as drug carriers since their properties can be adjusted without affecting the pharmacodynamics of the medication. Research is underway to utilize nanoparticle-mediated drug delivery to mitigate the adverse effects of chemotherapy (Peer et al., 2020). Conventional chemotherapy presents challenges related to unfavorable pharmacokinetics, toxicity, and non-specific tumor targeting. To effectively treat tumors, high doses are often required. However, the therapeutic benefits are constrained by the adverse effects of such large

<https://doi.org/10.1016/j.arabjc.2023.105267>

1878-5352/© 2023 The Author(s). Published by Elsevier B.V. on behalf of King Saud University.

This is an open access article under the CC BY-NC-ND license (<http://creativecommons.org/licenses/by-nc-nd/4.0/>).

doses (Rahman et al., 2007). In response to this situation, recent advancements in nanotechnology have been made, introducing chemotherapeutic nanoparticles that employ both active and passive targeting strategies to enhance therapeutic parameters for cancerous tissues simultaneously.

Biocompatibility is defined as the ability of a material to fulfill its intended function in medical therapies without inducing toxic, allergic, inflammatory, mutagenic, immune, or carcinogenic properties in the recipient of the therapy. Furthermore, it should elicit the most suitable beneficial tissue and cellular response in that specific context while addressing clinically relevant challenges (Harianawala et al., 2016). Radiolabeling of nanoparticles (NPs) is a valuable approach for imaging microorganisms with a high aspect ratio (Cadafalch Gazquez et al., 2016; Pijeira et al., 2022). However, after radiolabeling, a challenging task is to preserve the surface, physical, and chemical characteristics of nanomaterials to enable optimal biodistribution and cell uptake processes (Abd Elmaboud et al., 2019). This underscores the significance of nanomaterial properties and chemical manipulation (Lübbe et al., 2001; Avedisian et al., 2009). Additionally, nanomaterials possess the advantageous quality of sustainability, allowing them to retain their features even after radiolabeling.

A wide range of materials are utilized in radiolabeling and other biological applications. Doping or combining them with other substances helps enhance the material's potency and rigidity (Cadafalch Gazquez et al., 2016). Zirconia, with its remarkable mechanical qualities and exceptional strength, owes its robustness to its crystalline structures. It is biocompatible, bioinert, and non-resorbable. *In vivo*, zirconium-coated implants outperform untreated implants in terms of osseointegration. Osteoblast cells cultured on ZrO₂ exhibit strong adhesion and growth characteristics, as well as the ability to proliferate and differentiate (Pijeira et al., 2022). Zirconia is among the metal oxide materials known for their biocompatibility and effective surface qualities necessary for biomolecule immobilization, which is crucial for improved imaging (Abd Elmaboud et al., 2019; Lübbe et al., 2001; Avedisian et al., 2009).

Zirconia exists in different crystallographic forms, including cubic (c), monoclinic (m), and tetragonal (t) structures (Bukhari et al., 2018; Sengupta et al., 2019; Quintard et al., 2002). These allotropes are stable within specific temperature ranges. The monoclinic structure is stable below ~ 1170 °C, while the tetragonal structure is observed between ~ 1700 °C and 2370 °C. Above 2370 °C, zirconia adopts a cubic structure (Davar et al., 2013). Zirconia finds extensive applications in various industries, including the medical field, due to its excellent mechanical properties. The phase transition, where one phase of zirconia transforms into another, occurs at specific temperature ranges. Tetragonal zirconia exhibits higher hardness and strength compared to other materials and is commonly used in applications requiring high strength and stiffness. However, when tetragonal phase undergoes a transition to the monoclinic phase it results in a 3–5 % increase in volume, formation of fissures, and a reduction in hardness (Hbaieb, 2012; Kelly and Denry, 2008). Nevertheless, doping zirconia with a small concentration of iron oxide has been shown to enhance its mechanical properties without inducing any secondary phase. To maintain the stability of the tetragonal (t) phase at lower temperatures, ions such as Fe³⁺, Y³⁺, Fe²⁺, are used in the treatment. It is important for the material to exhibit both compatible optical response and mechanical strength. When tetravalent atoms replace trivalent or divalent atoms, metal oxides tend to develop oxygen vacancies (Imran et al., 2019; Sundell et al., 2006).

Iron oxide is employed as a stabilizer due to its proven biocompatibility and its ability to preserve the mechanical strength of zirconia (Guo and Xiao, 2012; Jain et al., 2008). Fe₃O₄-doped zirconia exhibits ferromagnetic properties and low coercivity, making it

suitable for biological applications (Imran et al., 2021; Mittal et al., 2022). Additionally, iron oxide enhances the development mechanism and stability process of zirconia without undergoing phase conversion (Zhukovskaya and Strakhov, 1980). Honey is a nutrient-dense, viscous, carbohydrate-rich fluid that is well-known for its disinfectant and pain-relieving properties. It has been utilized for its medicinal properties and healing purposes (El-Kased et al., 2017). Honey consists of various biomolecules and has been employed by multiple research groups for the synthesis of different nanoparticles (Philip, 2009; Balasooriya et al., 2017; Venu et al., 2011; Heshmatpour and Aghakhanpour, 2011). Various methods have been employed to produce zirconia doped with metal oxides, such as laser ablation (Han et al., 2022), RF sputtering (Smeacetto et al., 2010), and the sol-gel technique (Jodłowski et al., 2018). Among these processes, the sol-gel approach is widely preferred due to its cost-effectiveness and ability to operate at moderate thermal temperatures. The sol-gel process begins with material hydrolysis to generate a sol, followed by condensation and drying to obtain a gel. Subsequently, the gel is thermally treated under inert atmospheric conditions to yield the final product (Bokov et al., 2021).

Kao et al., (Kao et al., 2018) checked the effect of iron oxide in yttria-stabilized ZrO₂ by mixing these powders using ball milling. Holz et al., (Holz et al., 2018) studied the effect of low Fe₂O₃ concentrations on the mechanical strength of stabilized zirconia using yttria. Zhao et al., (Zhao et al., 2010) fabricated the ZrO₂ nanofibers by electro spinning process. The mean diameter of zirconia nanofibers was observed to be 80 nm after calcination at 400 °C. Tetragonal zirconia phase was observed after calcination at 400 and 600 °C. Stabilized zirconia nanofibers were prepared by reactive sol-gel electro-spinning process as reported by Xu et al., (Xu et al., 2010). YZ exhibited tetragonal phase after calcination from 500 °C to 1400 °C. Yuan et al., (Yuan et al., 2022) synthesized ZrO₂ NPs using a green approach utilizing *P. nirurui* leaf extract. DLS analysis indicated that the average particle size of ZrO₂ NPs was 121.5 nm with a negative zeta potential of 22.6 mv. Muthulakshmi et al., (Muthulakshmi et al., 2023) used *Guettarda speciosa* (*G. speciosa*) leaf extract to produce zirconia nanoparticles. Kadiyala et al., (Kanth Kadiyala et al., 2023) green synthesized zirconium oxide nanoparticles, i.e. ZrO₂/rGO NCs and tested biocompatibility. In previous studies, variety of stabilizers, i.e. yttria, magnesium oxide and calcium oxide, have been used to stabilize/partly stabilize ZrO₂ nanoparticles by obtaining tetragonal phase (Li et al., 2020; Cao et al., 2022; Lu et al., 2022). However, high temperatures were required to achieve stability (Peng et al., 2018).

The objective of the current study is to investigate the structural, mechanical, and magnetic properties of stabilized zirconia nanoparticles with varying concentrations of Fe₃O₄. The concentration of Fe₃O₄ was increased from 1 to 10 (wt. %). XRD analysis was performed to determine the phase purity of the synthesized samples. Vibrating sample magnetometer (VSM) results were utilized to confirm the magnetic nature of the samples, demonstrating their potential for cancer diagnosis and treatment. Optimized nanoparticles were subsequently employed for biodistribution studies in rabbits. Radiolabeling was achieved by utilizing sodium pertechnetate (Na^{99m}TcO₄), eluted from the PAKGEN ⁹⁹Mo/^{99m}Tc generator.

1.1. Hypothesis statement

Present research work is designed to explore the optimization of stabilized zirconia without using toxic stabilizers. Low cost sol-gel method will be used for synthesis purposes. This material will be optimized by keeping in mind its bio-activity and biocompatibility for future biomedical application. *In-vitro* and *in-vivo* both approaches will be used to check the compatibility and efficiency level of synthesized material.

1.2. Clinical significance

It's been predicted that the honey added Fe₃O₄ stabilized ZrO₂ nanoparticles can act as multifunctional material. Synthesized material under optimized conditions can be used for diagnostic as well as therapeutic purposes. Optimized nanoparticles can be used for effective drug loading and releasing purposes. Effective biodistribution of these nanoparticles can help in diagnosing as well as targeting the cancer cells based on obtained *in vitro* and *in vivo* results.

2. Experimental details

2.1. Materials and method

Zirconium oxychloride octa hydrate (Sigma–Aldrich with 99.99% purity), Fe(NO₃)₃·9H₂O (Sigma–Aldrich with 99.99% purity) were utilized without any further purification. Distilled water was doubly deionized (D.I.) before usage. Honey (natural sweetener) was collected from honeybee hive from Botanical garden of University of the Punjab, Lahore.

For preparation of zirconia sol, ZrOCl₂·8H₂O was utilized as precursor, while D.I. water was used as solvent to prepare 0.1 M solution (Sol I). After this, pre-synthesized sol of iron oxide (Fe₃O₄) at pH 9 having molarity of 0.1 M was used as a stabilizer. Detailed preparation for ZrO₂ and Fe₃O₄ sol is reported elsewhere (Sanaullah et al., 2021; Sanaullah et al., 2021; Bashir et al., 2015; Khan et al., 2023). Various concentrations, i.e. 1 to 10 wt%, of Fe₃O₄ sol were added in 0.1 M solution of zirconia. Detailed study of iron oxide stabilized ZrO₂ has been previously reported (Khan et al., 2023). After synthesis of iron oxide stabilized zirconia sols, 1 ml of honey was added to 100 ml of synthesized solution. Sols of all the samples prepared at various concentrations of iron oxide were dried at temperature of 80 °C to form powder. Synthetic route for stabilized nanoparticles is expressed in the form of a flow chart in Fig. 1.

2.2. Radiolabeling of zirconia nanoparticles

These synthesized zirconia nanoparticles were tested for radiolabeling and biodistribution (scintigraphy) studies. Radiolabeling was performed by using sodium pertechnetate (Na^{99m}TcO₄), eluted from PAKGEN ⁹⁹Mo/^{99m}Tc generator, which is locally-produced in Pakistan. The chemicals utilized in this research work were obtained from Sigma–Aldrich. The animal/rabbit trials were accomplished after getting approval from the Animal Ethical Board of INMOL Hospital. The protocol for biodistribution of radiotracer in animal models has been developed at INMOL lab after a series of experiments on various radiopharmaceuticals, keeping in view the blood pool formation, uptake of radioconjugate in various body organs (biodistribution), its retention in those organs and excretion pattern from the body.

2.3. Synthesis of labelled zirconia nanoparticles

^{99m}Tc was used to radiolabel zirconia nanoparticles (IOZH). As an experimental procedure, the Tc-99 m metal was reduced by using 20–40 µg of SnCl₂·2H₂O at a pH value between 4 and 7, which was fixed using either 0.1 M NaOH or 0.1 M HCl. To get maximum labeling yield, the amount of zirconia nanoparticles varied from 0.25 mg to 0.75 mg. The optimized radiolabeling conditions were 0.5 mg of zirconia nanoparticles dissolved in 20 µL of D.I water, in presence of 40 µg of SnCl₂·2H₂O at pH value of 4. For radiolabeling, ~370 MBq ^{99m}TcO₄ (equivalent to 10 mCi in saline) was

added in reaction vial and incubation of vial was done for about 25–30 min at 24 ± 2 °C.

2.4. Quality control

Ascending paper chromatography was employed to evaluate radiochemical yield (% labeling efficacy) of ^{99m}Tc-zirconia nanoparticles. The content of free ^{99m}TcO₄⁻ present in radiolabeled nanoconjugate was evaluated using Whatman chromatography paper # 3 in saline and acetone as stationary and mobile phase respectively. In this experimental setup, the amount of free ^{99m}TcO₄⁻ moved along solvent front and ^{99m}Tc-zirconia nanoparticles reside at the base level. The content of radiocomplex and free ^{99m}TcO₄⁻ was determined by dividing the chromatography strip into 1 cm fractions. The radioactivity was counted on gamma-counter (SCALER TIMER ST7). The amount of the colloidal content was measured by passing the radioconjugate through a 0.22 µm filter. In order to obtain the radioconjugate as a potential radiotracer, we tested its stability till 24 h at room temperature.

2.5. Stability of labelled zirconia nanoparticles

After attaining the radiolabeling parameters, the stability of labeled nanoconjugate was tested by incubating it at room temperature till 24 h. The estimation of free and colloid complex at various time intervals, e.g. 2, 4 and 24 h of incubation was assessed by using ascending paper chromatography.

2.6. Lipophilicity test and protein binding of labelled zirconia nanoparticles

Human blood plasma (obtained with prior approval from a healthy volunteer) was used to investigate *in vitro* protein binding. To initialize the procedure, 1.5 ml of human blood plasma and 500 µL of radiolabeled complex were mixed to form a slurry and then incubation of this slurry was performed at the temperature of 37 °C for a time period of 1 h. Following incubation, the mixture was separated (in blood serum and human blood cells) by centrifuging it at 3000 rpm for 10 min. The supernatant layer was combined with an equivalent amount of trichloroacetic acid before being centrifuged for 10 min at 3000 rpm. Centrifugation was performed to get the separate layers so that gamma camera could be used to measure obtained radioactivity. All studies were carried out in triplicate.

Lipophilicity is directly associated with the partition coefficient (p) measurements in-between the organic layer and aqueous layer. It was determined by performing incubation of 80 µL of the radiolabeled complex with 200 µL of phosphate buffer having pH values of 6.6, 7.0, and 7.6. Afterwards, 200 µL of n-octanol was transferred to each vial, and the three vials were shaken for around a time period of 10–15 min for the separation of two distinct layers. The radioactivity content of each layer was quantified with a gamma counter after separation.

2.7. Stability in human blood serum

To test the stability of a new radioconjugate in normal human sera, 1 ml of serum was incubated at 37 °C with 200 µL of radioconjugate. The stability was assessed by extracting an aliquot from the sample at various time periods up to 24 h during incubation. The radiolabeling effectiveness was assessed once again using paper chromatography, as previously described. Any reduction in radiolabeling yield might be due to radiolabeled conjugate degradation.

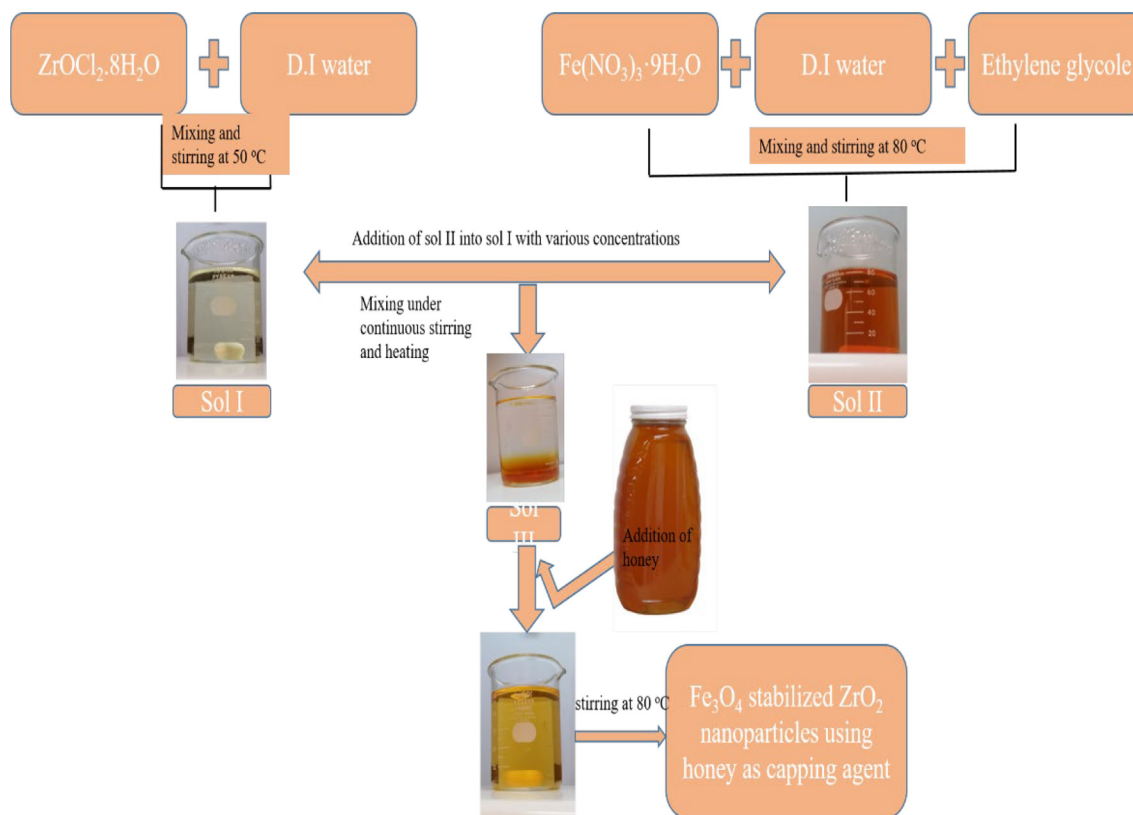


Fig. 1. Flow chart of the synthesis of iron oxide stabilized.

2.8. Labelled zirconia nanoparticles scintigraphy study in rabbit

To assess the practicality of a new nano-radioconjugate as a radiopharmaceutical medicine, we administered it intravenously (in the posterior ear vein) to rabbit models and acquired pictures using a single-headed gamma imaging camera. It was linked to an internet computer (carrying Macintosh operating system 7.5 and an ICON™ Workstation) through a spatial fidelity parallel-hole collimator. As part of the experiment, the animal was housed on a level hard surface with both back legs extended wide and all four legs taped using surgical tape. The local anesthesia was established by infusing 2 ml of Diazepam intramuscularly through the left thigh. The radioactive medication to be examined, for example 130 MBq (in 300 μ L) of ^{99m}Tc -zirconia nanoparticles, was administered intravenously into the animal's marginal ear vein. Photos were taken at 10 min in dynamic view, followed by static photographs after 10 min, 2 h, 4 h, and 24 h after the injection to investigate the biodistribution of tracer in animals.

2.9. Characterization tools

To analyze the crystalline nature and structure of produced nanoparticles, an X-ray diffractometer with a Cu K-alpha radiation source was used. The mechanical properties of the zirconia samples were determined using a Shimadzu HVM-2 Vickers micro indenter in accordance with ASTM C1327-99 (American Society for Testing of Materials, 1999). Wayne Kerr Precision 6500B impedance analyzer was used to test the dielectric characteristics of as generated samples. To test the magnetic characteristics of the samples, a LakeShore vibrating sample magnetometer (VSM) (Series 7400 and model 7407) was used. DPPH (2, 2, diphenyl-1-picrylhydrazyl) method was applied to investigate anti-oxidant

activity and to measure absorption intensity, Shimadzu UV-1800 UV-visible spectrophotometer was employed. The biodistribution of tracer in animals was studied using a single-headed Siemens optimized ORBITER gamma camera system (rabbit).

3. Results and discussion

Fig. 2 illustrates X-ray diffraction (XRD) patterns of ZrO_2 nanoparticles stabilized with various concentrations of Fe_3O_4 . The diffraction peaks i.e. $\sim 24.40^\circ$, $\sim 31.77^\circ$, 40.31° , $\sim 48.53^\circ$ and $\sim 64.48^\circ$ corresponding to (-110) , (111) , (-211) , (022) and (032) planes (card no. 00-013-0307) indicated the formation of monoclinic entities in as synthesized nanoparticles. While, peaks appearing at angles of 30.58° , 35.56° , 42.53° , 53.84° , 62.31° & 73.28° are due to (111) , (200) , (112) , (221) , (222) and (400) planes of tetragonal phase of zirconia respectively [card no. 00-017-0923].

The crystallite size (D) was measured by mean of Williamson-Hall plot as expressed in Eq. (1) (Cullity, 1956):

$$\frac{2\omega_f \cos \theta}{K\lambda} = \frac{1}{D} + \frac{4e}{K\lambda} \sin \theta \quad (1)$$

Here, $2\omega_f$ is measured in radians, K is utilized to show shape factor, wavelength is expressed as λ , produced microstrains in the samples is expressed by e ($=\Delta d/d$) factor, D particularizes the size of crystallites and θ is used to demonstrate Bragg angle.

To calculate dislocation density (δ), following expression was used (Eq. (2) (Cullity, 1956).

$$\delta = \frac{1}{D^2} \quad (2)$$

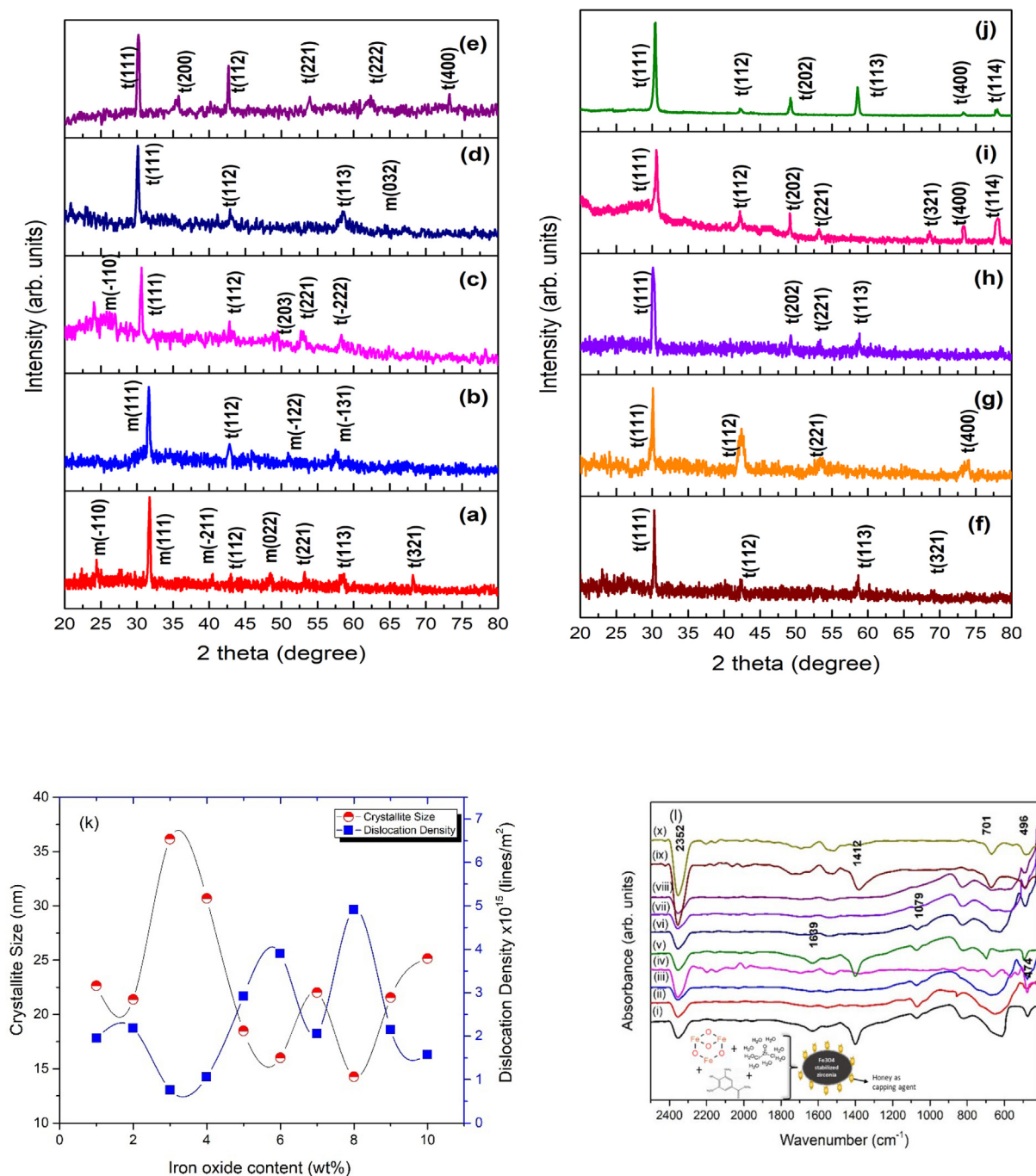


Fig. 2. XRD patterns of nanoparticles with iron oxide content of (a–j) 1–10 wt% and (k) crystallite size and dislocation density, (l) FTIR spectra of as synthesized nanoparticles using various concentration of iron oxide as a stabilizer.

Crystallite size and dislocation density, as estimated from the Eq. (2), are plotted as a graph with altering the concentration of iron oxide as depicted in Fig. 2(k). The Fourier transform infrared spectra of Fe₃O₄ stabilized ZrO₂ nanoparticles are shown in Fig. 2(l).

The morphological features of nanomaterials (size, shape, and roughness) have been observed to impact their applications, making microscopic examination a valuable tool in determining the nature of a nanomaterial. SEM micrographs, as shown in Fig. 3, show uniform large area growth of zirconia samples synthesized under different conditions, i.e. variation in iron content.

For bio-medical applications, the functional material's adsorption on the surface of nanoparticles and hydrodynamic diameter

size of particles plays a crucial role. The size of nanoparticles determined by DLS procedure helps in understating the adsorption of molecules on the surface of nanoparticles. Zetasizer (Nano ZEN3600, Malvern Instruments, UK) was used in the present study to check the hydrodynamic diameter size along with the potential values. Average zeta size and PDI of as synthesized nanoparticles are given in Table 1. Fig. 4(a–j) shows the average zeta size value of synthesized nanoparticles. The zeta potential is also an important parameter for a biomaterial surface, since it affects the protein adsorption (Cai et al., 2006), cell attachment (Cheng et al., 2005) and bacterial adhesion (Gottenbos et al., 2001) in a physiological environment. The stability of ZrO₂ nanoparticles can be assessed by the zeta potential measurements (Jameel et al., 2020). Examin-

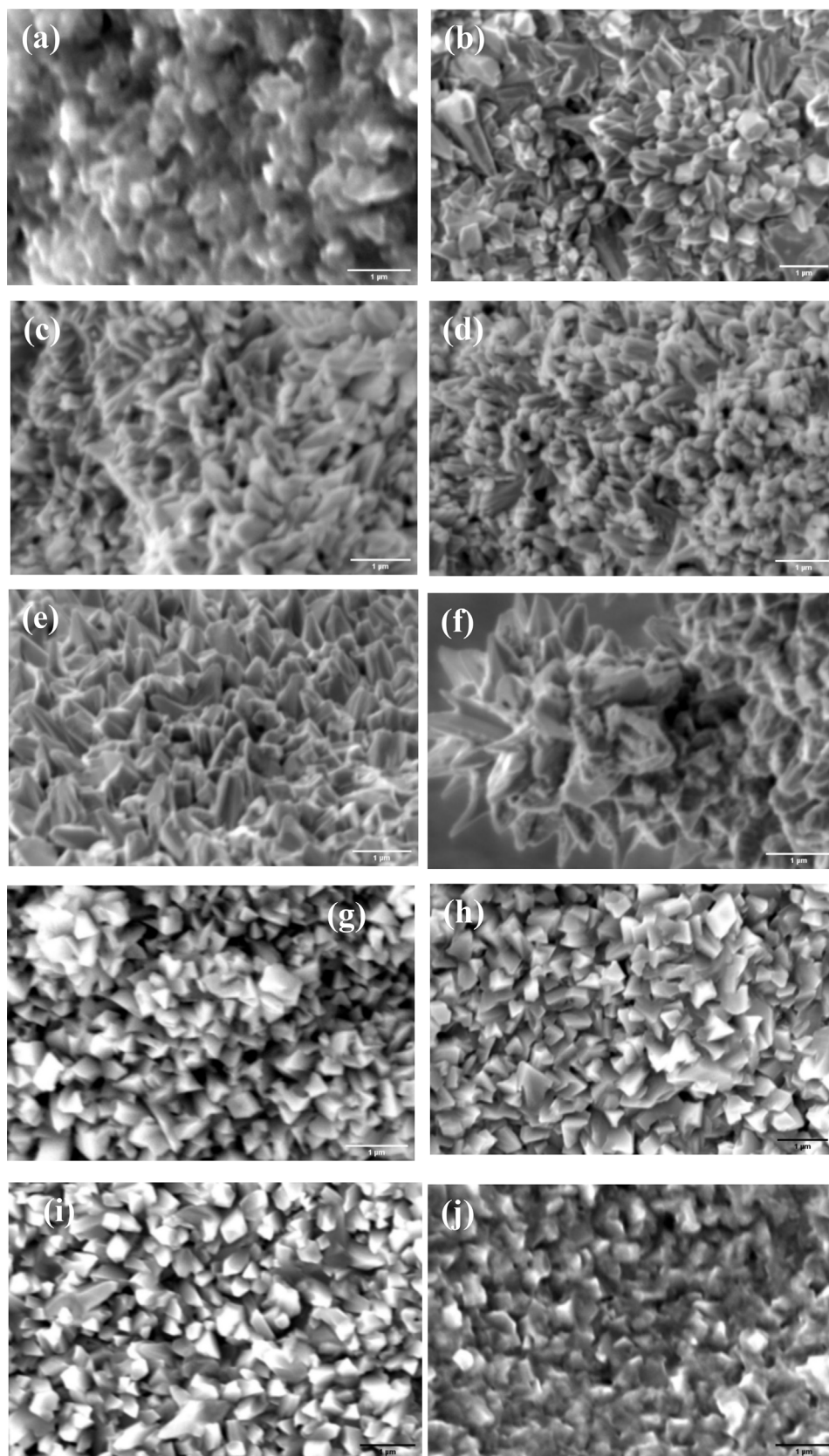


Fig. 3. SEM images of zirconia stabilized with iron oxide content of (a-j) 1–10 wt%.

ing the zeta potential helps to better understand the comprehensive characteristics of nanoparticles for their biomedical applications. Suriyaraj et al., (Renger et al., 2004) demonstrated zeta potential of 36.5 ± 5.5 mV for ZrO_2 . Chau et al., (Chakravarty et al., 2010) reported zeta potential of -32.8 mV for ZrO_2 nanoparticles biosynthesized from *Laurus nobilis* leaf extract.

Table 1

Average zeta size and PDI of as synthesized nanoparticles.

Sample name	Z average (d.nm)	PDI (polydispersityindex)
(a)	423.0	0.372
(b)	535.9	0.651
(c)	828.4	0.825
(d)	322.1	0.527
(e)	1127	0.892
(f)	291.4	0.610
(g)	420.6	0.632
(h)	372.8	0.622
(i)	398.4	0.535
(j)	359.7	0.618

Nanoparticles consisting of magnetic oxides, like magnetic iron oxide (Fe_3O_4), are very useful for the purpose of imaging as well as separation techniques. Due to their biological and chemical inertness, they are frequently used as a coating material to increase functionality of antibodies or enzymes as separation agents. To utilize zirconia nanoparticles stabilized using Fe_3O_4 , it is very crucial to find out their magnetic behavior as for biomedical applications magnetic properties play an important role. MH loops of synthesized nanoparticles exhibited soft ferromagnetic behavior as shown in Fig. 5.

It is essential to look into the impedance capabilities of materials that is to be used as regrow/repair bone tissue and biological cells. These qualities may be greatly influenced by the applied or externally present field, influencing the behavior of nanoparticles. The suitable dielectric constant values are in the range of ~ 18 – 68 for biomedical applications at high values of frequency (Yentekakis and Chu, 2020; SanaUllah et al., 2022). The impedance response of IOZH nanoparticles was thoroughly investigated. The room temperature behavior of all samples generated with varying iron oxide concentrations was investigated. Capacitance and resistance were obtained by means of impedance analyzer. Frequency dependent

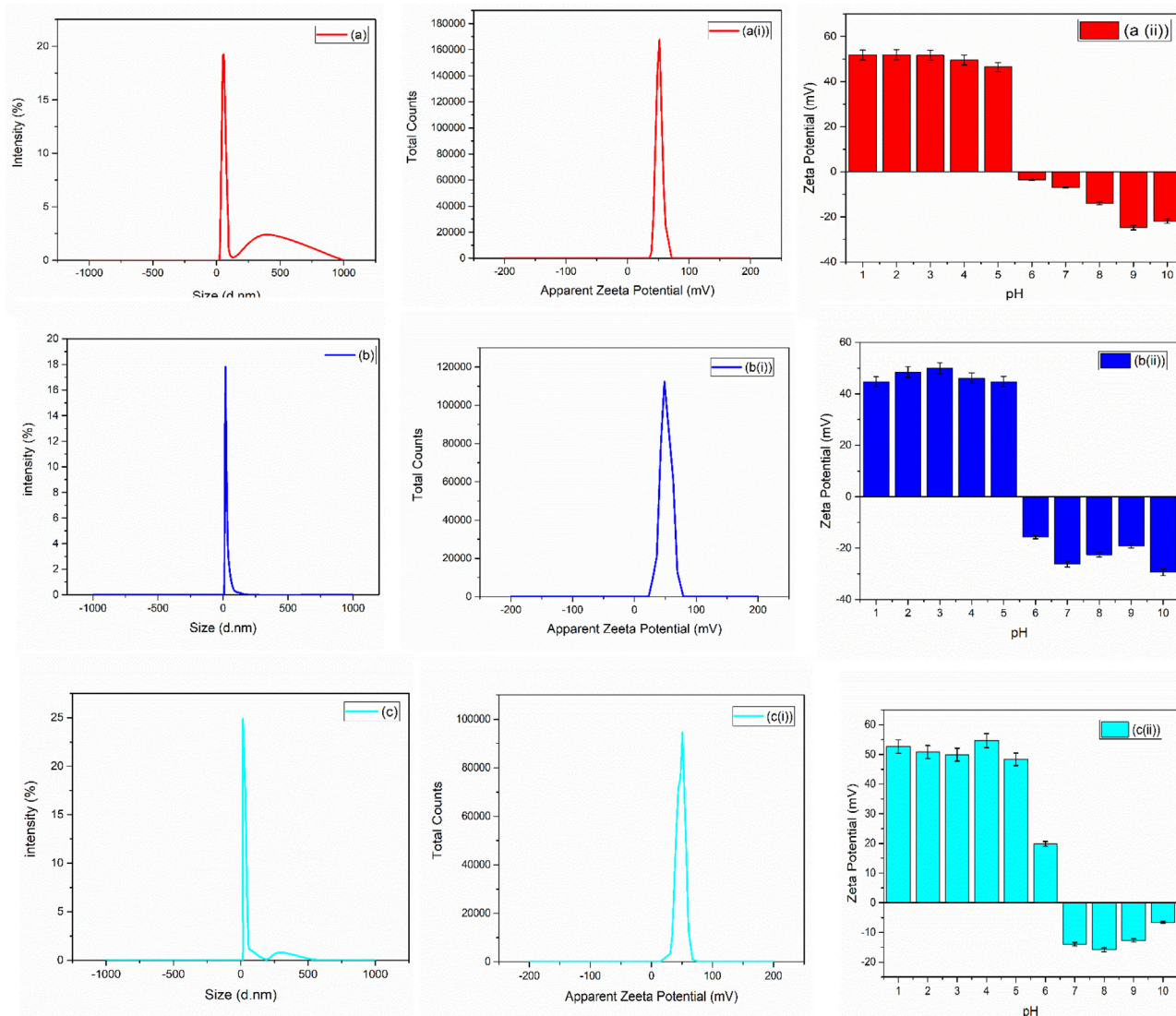


Fig. 4. (a–j) average zeta size, (a(i)–j(i)) average zeta potential and (a(ii)–j(ii)) average zeta potential of zirconia nanoparticles at various pH of zirconia nanoparticles using 1–10 wt% of iron oxide.

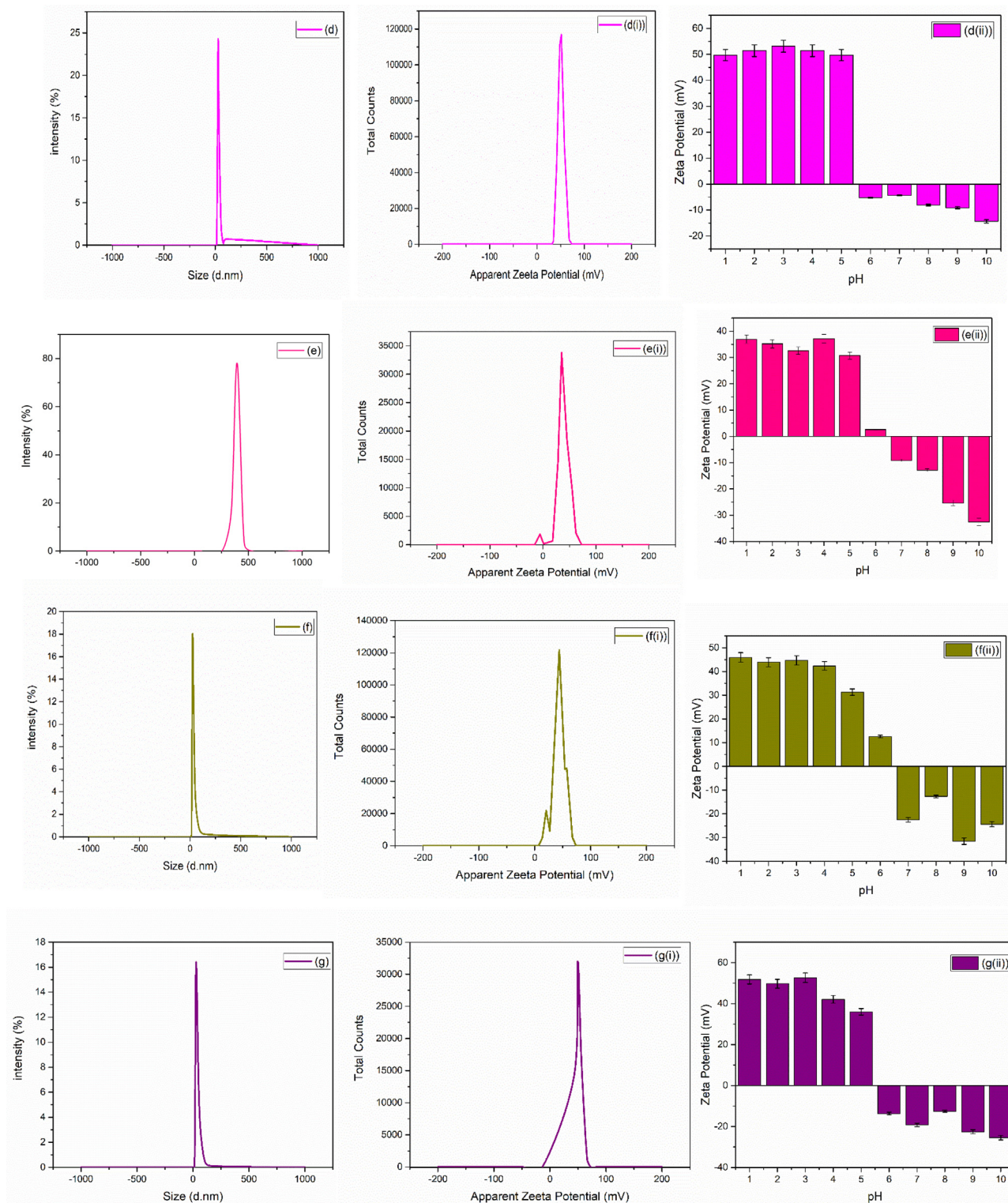


Fig. 4 (continued)

response of dielectric constant (ϵ) and tangent loss ($\tan\delta$) were obtained from Eqs. (3) and (4) (Macdonald and Barsoukov, 2005).

$$\epsilon = (Cd)/\epsilon_0 A \tag{3}$$

$$\tan\delta = 1/(2\pi f \epsilon \epsilon_0 \rho) \tag{4}$$

Where

C = capacitance by mean of parallel plate configuration; d = thickness of the prepared sample; A = area ; ϵ_0 = free space permittivity; ρ = resistivity; f = frequency.

Fig. 6 depicts a decrease in the value of the dielectric constant along with tangent loss with increment in frequency, displaying typical dispersion behavior.

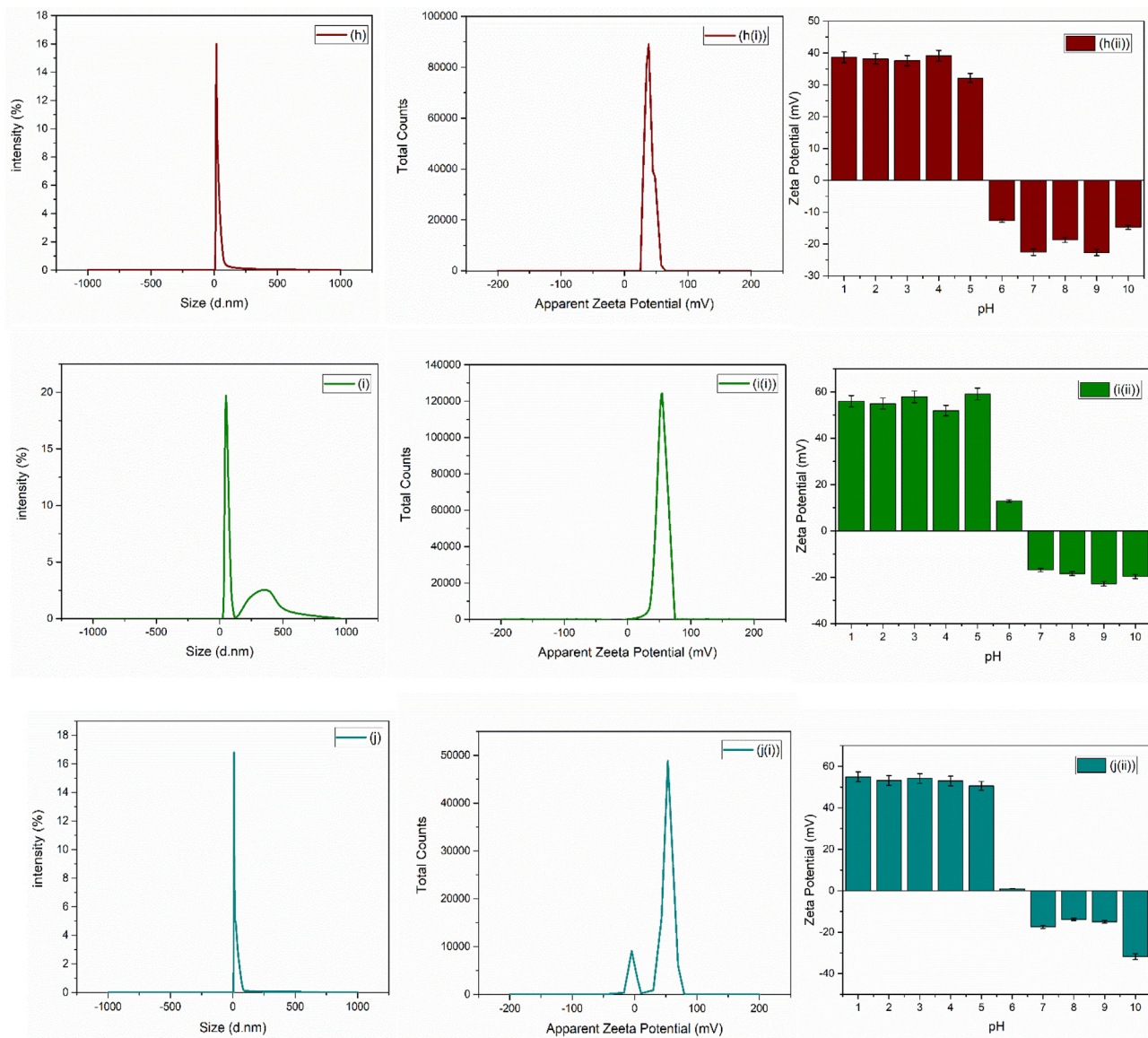


Fig. 4 (continued)

The hardness of material is a key component that describes its potential use under various atmospheres.

Fig. 7 (a-f) displays the hardness value at a total of $2500 \mu\text{m}^2$ of microstructural sites. The hardness maps were created by combining image data from a Shimadzu HMV-2 Vickers micro indenter and Origin software (Origin (Pro), 2016, OriginLab Company, Northampton, USA). Indentation displays random values in each position due to the varied and random orientation of each grain hardness value. That's the main reason that each region of sample prepared using nanoparticles displays a dissimilar/distinct mechanical property as also shown by mean of color filled contour plot even after using same dwell time and force, i.e. 4.903 N load for 15 sec according to ASTM C-1327.

Simulated body fluid (SBF) based test was utilized to investigate colloidal stability as well as biodegradability of as synthesized samples as used previously (Pattnaik et al., 2011). Nanoparticle based compressed round shape discs were submerged in SBF for a time period of 1, 2, 4, 8, 13, 20, and 26 weeks. The area (mm^2), diameter (mm), and thickness (mm) of the compacted disc were measured, before starting the submersion. Biodegradation results of samples are shown in Fig. 8(a).

Fig. 8(b) shows the labelling efficacy of curcumin. An ethanolic solution containing curcumin ($200 \mu\text{g}/\text{mL}$ having pH 7) was set up to evaluate the drug (curcumin) loading efficacy of IOZH. The curcumin solution was formerly incorporated with IOZH nanoparticles, and the slurry was agitated for 2 h at room temperature in the dark (25°C) (Janes et al., 2001; Farahani et al., 2020; Mohanty et al., 2010). Centrifugation was used to dry drug-load nanoparticles after stirring. The IOZH nanoparticles were further treated at least 3–4 times with ethanol to neutralize the unbound medicine i.e. curcumin. After washing, the curcumin-loaded stabilized IOZH nanoparticles were heated for 5 h at 50°C .

To evaluate the scavenging capability of as synthesised IOZH nanoparticles against reactive oxygen species, DPPH assay was utilized (Das et al., 2013), (Serpen et al., 2007; Shin et al., 2017). Methanolic stock solution of IOZH nanoparticles were prepared to make working solutions having concentrations from 50 to $250 \mu\text{g}/\text{mL}$ (with an interval of $50 \mu\text{g}/\text{mL}$). Further this working solution was added into 1 ml of methanolic DPPH solution (1 mM). The same amount of ascorbic acid was utilized as a positive test control. Scavenging capability of samples is shown in Fig. 8(c).

To evaluate the *in-vitro* anticancer capability of as synthesized IOZH nanoparticles through MTT assay, HCT-116 cell lines (colon cancer cells) were cultivated in DMEM (Dulbecco's Modified Eagle's Medium) along with 10% heat-inactivated FBS (fetal bovine serum) and antibiotic (penicillin) (Balaji et al., 2017 and Rajapriya et al., 2020). The incubation took place at 37 °C with 5% CO₂ vapor present. To assess the vitality of optimized samples, the MTT test was utilized. Fig. 8 (d) depicts the proclivity of customized nanoparticles to diminish the cell viability (%) of colon cancer cell lines (HCT-116). When the concentration of ideal sample of as generated nanoparticles grew, the percentage of cell viability declined continuously. A concentration of 5 to 25 µg/mL (with 5 µg/mL interval) was utilized as working solution.

The antibacterial activity of the nanoparticles (prepared with 5-10wt%) was performed using standard agar well diffusion. The *in vitro* antibacterial activity studies was performed against 24-h

culture of bacterial strains *Bacillus subtilis* (taken from Institute of MicroBiology & Molecular Genetics, University of the Punjab, New campus, Lahore, Pakistan). Petri plates containing 20 ml nutrient agar were prepared and wells were formed. Bacterial strains were swabbed into petri dishes. Varying concentrations (5-25 µg/ml) of nanoparticles were added to check the antibacterial response (Manjunatha et al., 2021). Zone of inhibition was measured in mm and recorded after 24 hours of incubation at 37°C as shown in Fig. 9 (a-f). Measured zone of inhibition (mm) are listed in Table 2.

Fig. 10 shows the results obtained from gram staining. Fig. 10(a) shows staining results for untreated bacterial strains. While Fig. 10(b-g) represents gram staining of nanoparticles treated bacteria. For nanoparticle treated bacteria, plates shown in Fig. 10 were utilized. Smear bacterial culture was taken from extreme edge of 20 µg/mL zone of inhibition for each plates. In Fig. 10(a) it can be observed that cells present different sporulating stages i.e. unipolar and bipolar. The bacteria can be seen in the form of chains and stained positive. As the stress of nanoparticles increased the cells staining is affected and towards the negative behaviour. The mature spores were also observed at higher IOZH i.e. 10 wt%. The cells also tends to arrange either singly or in pairs at progression towards higher wt%.

Radiolabeling of zirconia nanoparticles includes an estimation of the radiolabeling yield, radiochemical purity and the stability of the radio-product. All of above said parameters were estimated through paper chromatography (in acetone as a mobile phase). In this chromatography system, free ^{99m}TcO₄ moved along the solvent (with R_f = 1) and the radiolabeled conjugate remained at the base line. To estimate the amount of colloid, the radioactive complex was filtered through a 0.22 µm filter and the content of radioactivity in filtrate and filter was measured in gamma counter which showed a negligible amount of colloid in final radio-formulation. Fig. 11 (a) shows the effect of pH on the radiolabeling yield.

Since the amount of reducing agent, e.g., SnCl₂·2H₂O plays a pivotal role in radiolabeling with Tc-99 m, so we studied the correlation between the amount of SnCl₂·2H₂O and the radiolabeling efficacy. Data are shown in Fig. 11 (b). The stability of ^{99m}Tc-zirconia nanoconjugate that reflects the rate of complexation was evaluated at room temperature. Results are shown in Fig. 11 (c).

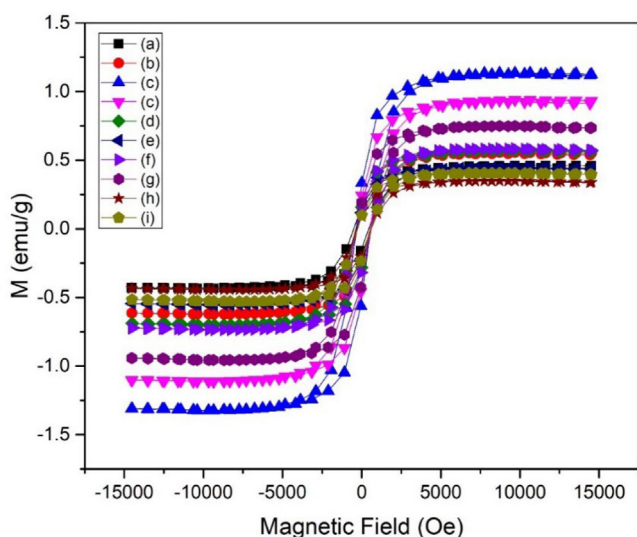


Fig. 5. MH curves of as synthesized nanoparticles using various concentration of iron oxide (a-j:1-10 wt%) as a stabilizer.

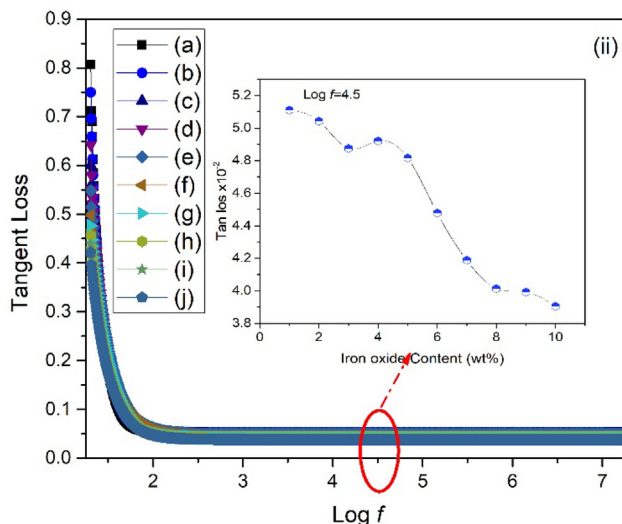
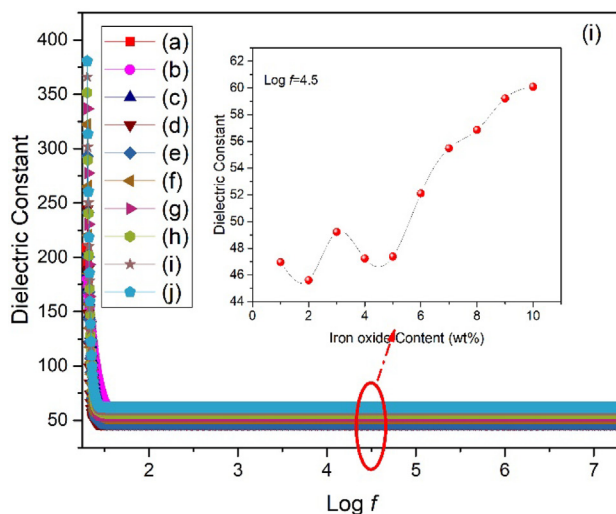


Fig. 6. (i) Dielectric constant and (ii) tangent loss of as synthesized nanoparticles using various concentration of iron oxide (a-j) 1-10 wt%. (insets show variation for all samples at fixed frequency).

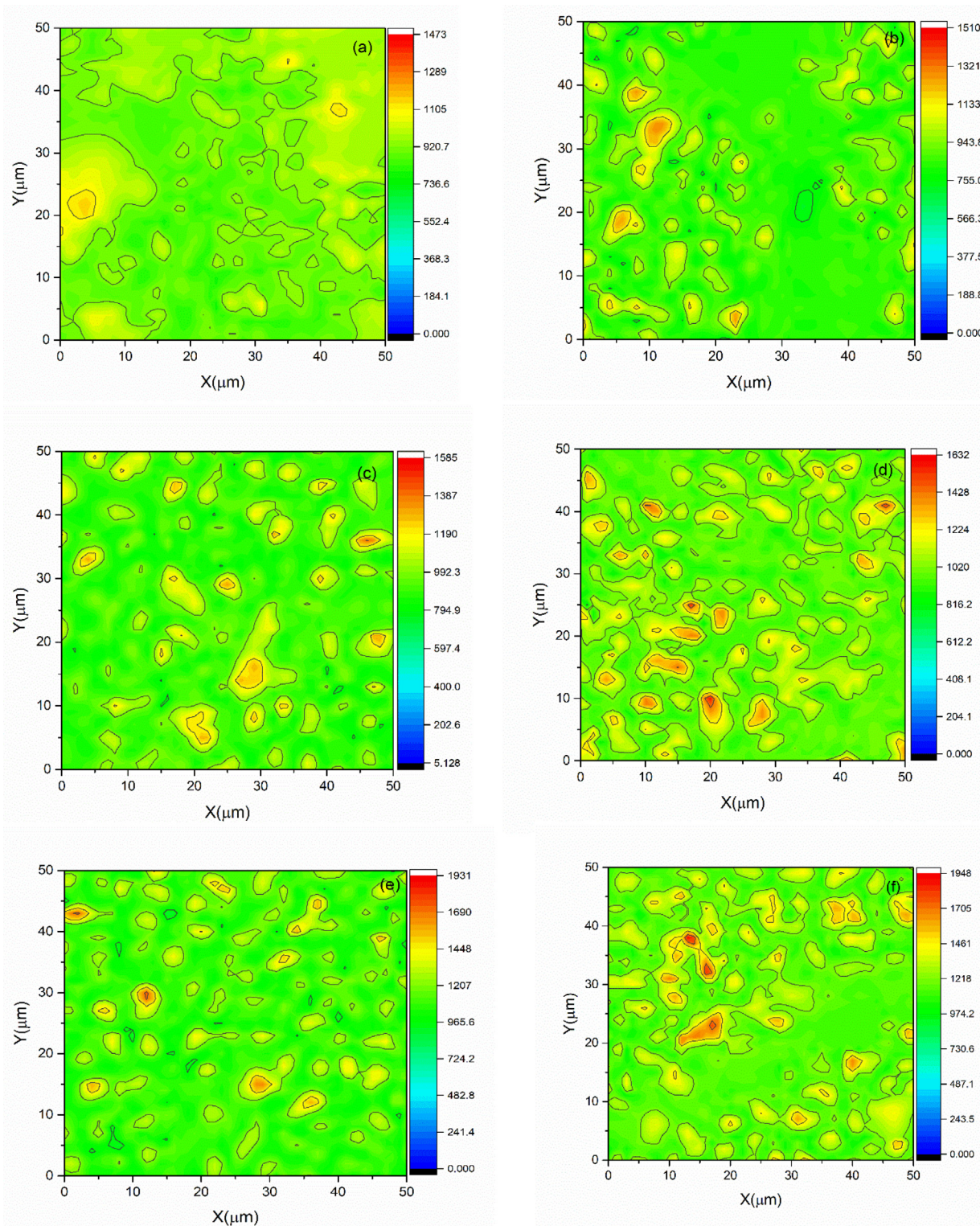


Fig. 7. Hardness mapping of samples with iron oxide concentration of (a-f) 5–10 wt%.

The stability of ^{99m}Tc -zirconia nanoconjugate was also evaluated in human blood serum as shown in Fig. 11 (d).

With these encouraging *in vitro* results in mind, the potential of ^{99m}Tc -zirconia nanoparticles was investigated *in vivo* by injecting it intravenously into a rabbit and generating its scintigraphy profiling on a Gamma Camera. After administering radiopharmaceutical

into rabbits, we analyzed the imaging in dynamic mode for 10 min (pictures at 1 min, 3 min, 4 min, 7 min, and 10 min) after injection (in anterior mode). Static photos were taken at 10 min, 1 h, 2 h, 4 h, and 24 h (p.i.) to clearly evaluate radiotracer accumulation in the animal; data are displayed in Fig. 12 (ii). Additionally, the rabbits were maintained under careful surveillance for 72 h following

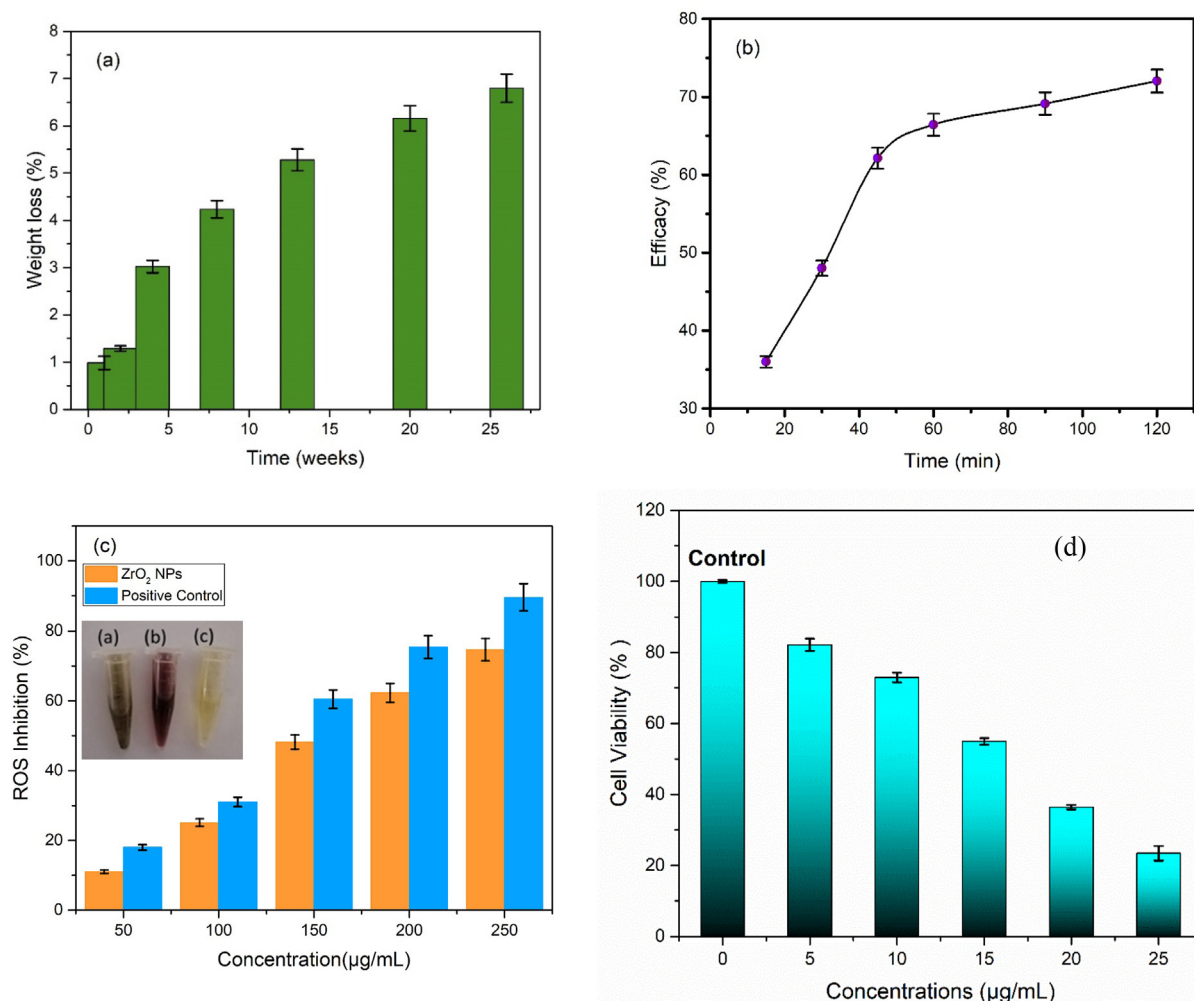


Fig. 8. (a) Biodegradation assay, (b) drug encapsulation efficacy, (c) ROS inhibition (inset shows color changing capacity of nanoparticles) and (d) cell viability capability of iron oxide stabilized zirconia nanoparticles.

the trial to identify any abnormalities. Fig. 12 (ii) depicts the absorption of ^{99m}Tc-zirconia nanoparticles in various animal tissues at several discrete time intervals.

The findings of scintigraphy data are supportive of the argument that uptake of a radioconjugate depends on several factors, e.g. nature of compound, pH value, lipophilicity and blood plasma protein binding level, etc. The high uptake value of ^{99m}Tc-zirconia nanoconjugate in the vital organs e.g. heart, liver, kidney and bladder [Fig. 13] indicates the potential of the novel radiocomplex to be further investigated, thus making these nanoparticles a potential nano-radiolabeled diagnostic agent.

4. Discussion

X-ray diffraction (XRD) results, presented in Fig. 2, showed formation of stabilized ZrO₂ nanoparticles under optimized conditions, i.e. the content of iron oxide. Monoclinic peaks of zirconia disappeared after increasing concentration of iron oxide from 5 to 10 wt%. Elimination of monoclinic phase is due to nucleation process which results after surpassing of super-saturation limit of stabilizer ions in the solution. A solid solution is formed in zirconium cation (Zr⁴⁺) and is replaced with ions of iron (Fe³⁺ or Fe²⁺). Because of the smaller sized atom replacement, oxygen vacancies are produced, which plays a crucial role in the stability of t-

zirconia even at low temperatures, which was previously unattainable. (Sanaullah et al., 2021; Tyagi et al., 2006; Cong et al., 2009). Honey was utilized during synthesis that may act as 1) capping agent, 2) reducing and 3) stabilizing agent (Bahari et al., 2023). Fructose and glucose are major moieties of honey. According to previous reports, fructose and glucose plays an important role for the reduction of OH⁻ ion (hydroxyl ions) as they have reducing nature (Cong et al., 2009; Sanaullah et al., 2020). It can be seen from Fig. 2(k) that nanoparticles had a lower crystallite size that was below 30 nm, particularly for 5 to 10 wt% of iron oxide content. It has formerly been shown that biologic implants as well as coatings exhibit little or no aggregation when the crystallite size is < 30 nm (Garvie et al., 1975). It has also previously been found that nucleation rates are inversely linked to crystallite size (Liu et al., 1995; Marsh, 1998). Due to existence of monomers in less quantity, crystallite size also reduces associated with rapidly occurring nucleation. As a result, nucleation rate plays a crucial role in controlling and restricting the Ostwald ripening process for controlled t-zirconia synthesis (Kelly and Denry, 2008; Sajjadi and Brooks, 2000; Sajjadi, 2007). Honey can be employed as a capping agent, which aids in the prevention of aggregation of ZrO₂ nanocrystals and has contributed significantly to the development of t-zirconia.

Fig. 2(l), i.e. FTIR spectra, shows that Zr-O-Zr bonds are prevalent in the 470–545 cm⁻¹ range. For 1–4 wt% of iron oxide, mixed

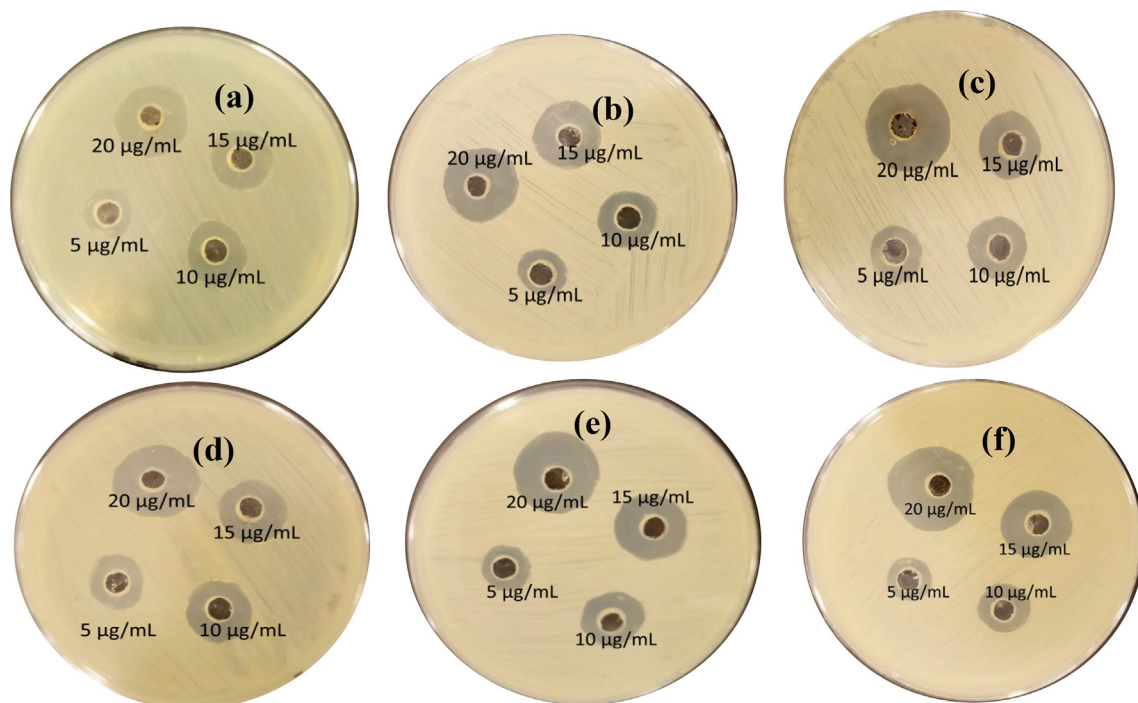


Fig. 9. Antibacterial activity of nanoparticles using iron oxide concentration of (a) 5 wt%, (b) 6 wt%, (c) 7 wt%, (d) 8 wt%, (e) 9 wt% and (f) 10 wt%.

Table 2

Antibacterial activity of nanoparticles using iron oxide concentration of (a) 5 wt%, (b) 6 wt%, (c) 7 wt%, (d) 8 wt%, (e) 9 wt% and (f) 10 wt%.

Nanoparticles concentrations	Sample name (zone of inhibition in mm)					
	(a)	(b)	(c)	(d)	(e)	(f)
0	-	-	-	-	-	-
5 µg/mL	9	10	10.5	11	11	11
10 µg/mL	12	12	13	14	14	15
15 µg/mL	13	15	14	15	16	17
20 µg/mL	19	20	20	21	21	22

bands (tetragonal and monoclinic) are visible. The bands at 470 cm^{-1} are likely due to a monoclinic phase fraction, but the band at 496 cm^{-1} is likely due to a tetragonal phase of zirconia. (Batool et al., 2020; Asha et al., 2019; Khalili and Chenari, 2020). For samples treated with high concentrations of iron oxide (5–10 wt%), the band (470 cm^{-1}) shifts towards higher wavenumber, which corresponds to tetragonal zirconia (496 cm^{-1}) as revealed by X-ray diffraction findings [Fig. 2(a-b)]. Many researches have previously documented the existence of t-ZrO₂ phase at this wavenumber (Sanaullah et al., 2021; Fang et al., 2013; Lopez et al., 2007). The conspicuous band at 2352 cm^{-1} is caused by O–H stretching of as-yielded nanoparticles. The band observed at 1639 cm^{-1} is because of the O–H stretching (Natalia et al., 2018). The peak at 1412 cm^{-1} corresponds to O–H bonding. While vibration bands present at 827 cm^{-1} are assigned to C = CH (Sahoo et al., 2011).

SEM images [Fig. 3] showed formation of hard agglomerated grains (Fig. 3(a–d)) for the samples with mixed structural phases. These hard agglomerated structures were observed because of the presence of multiple large numbers of tightly packed grains (Singh et al., 2017; Adeyemi et al., 2022) due the presence of two competing crystal phases. Large area growth with uniform surface morphology was observed with the increase in iron content from 5

to 10 wt% [Fig. 3 (e–j)]. Further, hydrodynamic diameter was also calculated and shown in Fig. 4. Various dilutions of zirconia nanoparticles were prepared in the present research work to investigate various parameters by adjusting pH using HCl and NH₃. Ultrasonication time of 20 min was used and process was repeated twice after cooling the solution. Analysis was performed in triplicate. Zeta potential of as synthesized nanoparticles are shown in Fig. 4(ai–ji). Variation in zeta potential with the change in pH values is shown in Fig. 4 (aii–jii). Fig. 4 shows a clear indication of pH dependent response of zirconia nanoparticles. Positive values of zeta potential were observed for acidic pH values (1–6). Whereas iso-electric point was observed with further increase in pH. Negative values of zeta potential were observed with the further increase in pH values to basic conditions. When the pH was 2, the zeta potential reached + $53.2 \pm 230\text{ mV}$, which gradually decreased to + $52.97 \pm 2.29\text{ mV}$ and + $0.95 \pm 0.04\text{ mV}$ with the increase in pH to 4–6. Further, 0 mV of zeta potential was observed at $\sim 6\text{ pH}$, and is known as the isoelectric point of the material under investigation. The stability of the nanoparticles in the form of solution fluid strongly depends on its pH nature (Nishakavya et al., 2022). For relatively higher pH values, i.e. 8 and 10, the value of zeta potential was increased to $-13.83 \pm 0.60\text{ mV}$ and $-31.8 \pm 137\text{ mV}$, respectively. These values might have been observed

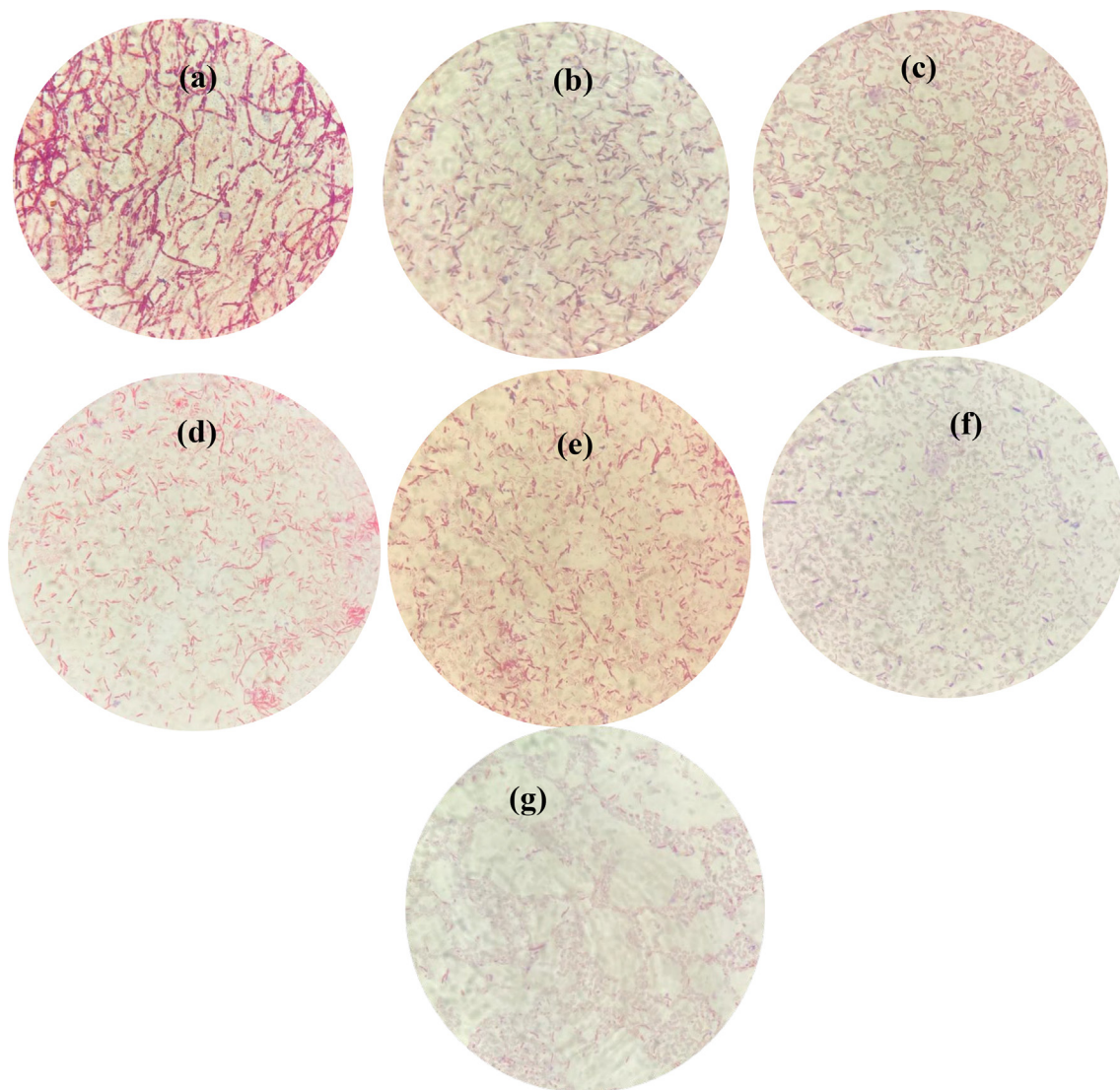


Fig. 10. Gram staining results of (a) untreated, IOZH using iron oxide concentration of (b) 5 wt%, (c) 6 wt%, (d) 7 wt%, (e) 8 wt%, (f) 9 wt% and (g) 10 wt%.

because of the charge value of oxide along with the dissociation of the hydroxyl groups present at the surface (Hiremath et al., 2021; Ordóñez et al., 2020).

Magnetization response of the samples were examined and plotted in Fig. 5. The observed soft ferromagnetic behavior can be attributed to the induced spin polarization by means of interaction due to attraction forces between host and doped electrons. The local electrons demonstrate similar direction of spin after the exchange interactions with polarized electrons of Fe^{2+} and Fe^{3+} ions (Xia et al., 2011). Therefore, because of these exchange interactions, ferromagnetic behavior was exhibited in the as synthesized nanoparticles. Honey was also added during synthesis, as a capping agent, and according to previous reports organic based molecules may exhibit magnetic ordering (Miller and Epstein, 1994; Miller, 2011). The presence of oxygen vacancies, as previously noted, results in the formation of t-zirconia. As the crystallographic phase changes from pure t- ZrO_2 to mixed zirconia, coercivity and saturation magnetization might change (Lin et al., 2018).

Dispersion phenomenon, as shown in Fig. 6, occurs after the introduction of an external electric field. It takes some time for these carriers to align in the direction of the externally applied field. As a result, these carriers have enough time to align at lower

frequencies. At higher frequencies, however, space charge carriers do not have enough time to respond, leading them to lag behind applied field and provide a lower dielectric constant value. Variation in dielectric constant with increment of stabilizer concentration may be related to particle size (SanaUllah et al., 2022; Gabriel et al., 1996). The increase in grain size with increasing iron oxide content promotes simpler domain wall motion, which results in an increase in the value of r . Furthermore, a larger concentration of iron oxide promotes the creation of a stronger intervening layer (insulator) near the grains. When compared to the resistance and capacitance of grain, these grain boundaries have a large resistance and capacitance (Ji and Brace, 2011; Jha, 2013). Because of the formation of mixed phases, a low dielectric constant value is achieved at lower stabilizer concentrations, as seen in Fig. 2. Meanwhile, increasing the concentration of stabilizer resulted in an increase in dielectric constant [Fig. 6(i)]. Relatively higher dielectric constant values are correlated with the stabilized zirconia samples [Fig. 2]. Figure S1 shows variation in real and imaginary impedance along with Cole-Cole plots. One semi-circle observed in Cole-Cole plots corresponded to a high frequency response of grains (Bukhari et al., 2018; Batool et al., 2020). At high concentrations of stabilizer, the area under the curve grows, indicating a higher value of impedance, whereas small semi circles

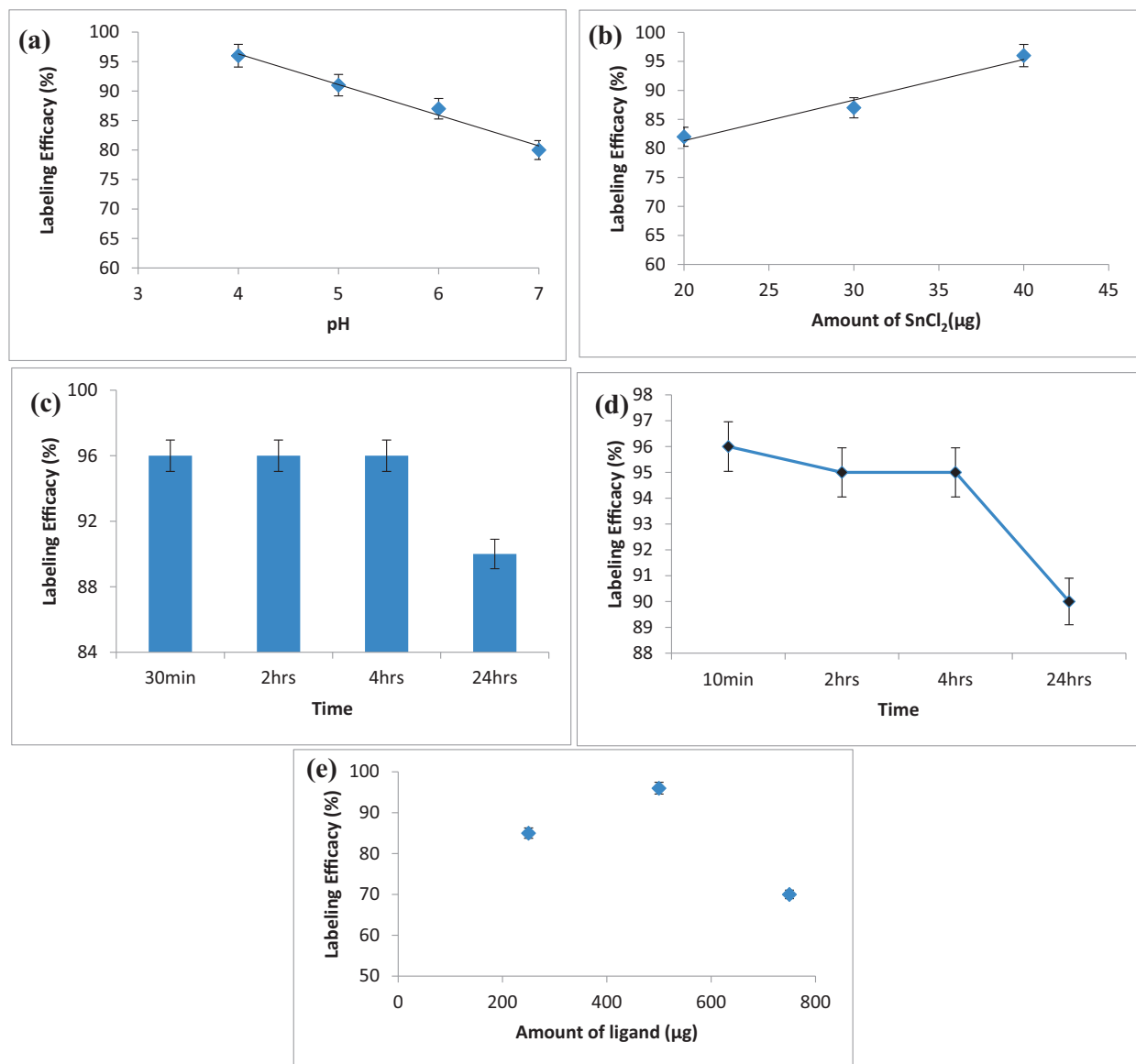


Fig. 11. (a) Effect of pH on radiolabeling efficacy, (b) Effect of amount of reducing agent on radiolabeling efficacy, (c) Stability of radiolabeled complex at room temperature, (d) Stability of radiolabeled complex in human blood Serum, (e) Effect of amount of the ligand on radiolabeling yield (%).

suggest a lower value of impedance. Materials with small grain size have a high amount of grain boundaries and consequently have a comparatively high hardness / mechanical strength.

Mechanical properties of synthesized material, shown in Fig. 7, is significant to switch/swap absorption routes while maintaining therapeutic effectiveness. Commonly, not only leakage is prevented due to the attracting force between liposomes and sample, but this force is also responsible for the modulation of pathway efficacy to penetrate. Samples with higher value of hardness can easily enter the cell wall by mean of endocytosis route. Because of shape distortion and non-uniform ligand distribution, soft NP might be hindered. (Sangtani et al., 2017; Dasgupta et al., 2017). Hardness is the property of a substance that resists the indent created by the applied force. Grain size has a significant impact on the hardness of the polycrystalline material. Materials with smaller grain sizes have bigger grain boundaries, resulting in better mechanical strength. A Vickers hardness micro-indenter was operated to assess the material's hardness along with the fracture toughness. An array of indentations in a 50 μm by 50 μm matrix was built to measure the homogeneity and uniformity of samples.

A contour map was employed to assess the mechanical behaviour of this matrix with an array of indents in terms of visual response.

The size of crystallites has a strong effect on the hardness of substance. The Hall-Patch equation, which is provided below as Eq. (5) (Niihara et al., 1982), can be used to correlate crystallite/grain size with hardness.

$$HV = (1.854)P/d^2 \quad (5)$$

Eq. (6) (Niihara et al., 1982) is used to calculate fracture toughness.

$$K_{Ic} = 9.052 \times 10^{-3} H^{3/5} E^{3/5} d.c^{-1/2} \quad (6)$$

Where

H is for Hardness in HV, E stands for Young's modulus, d stands for mean diagonal length of the indent, and c stands for mean length of the Palmqvist fracture. Increased value of fracture toughness, i.e. 20–24 MPam^{-1/2}, was observed for the samples prepared with 5–10 wt% of iron oxide content. Because of the presence of the dominating monoclinic phase and high grain size values, sam-

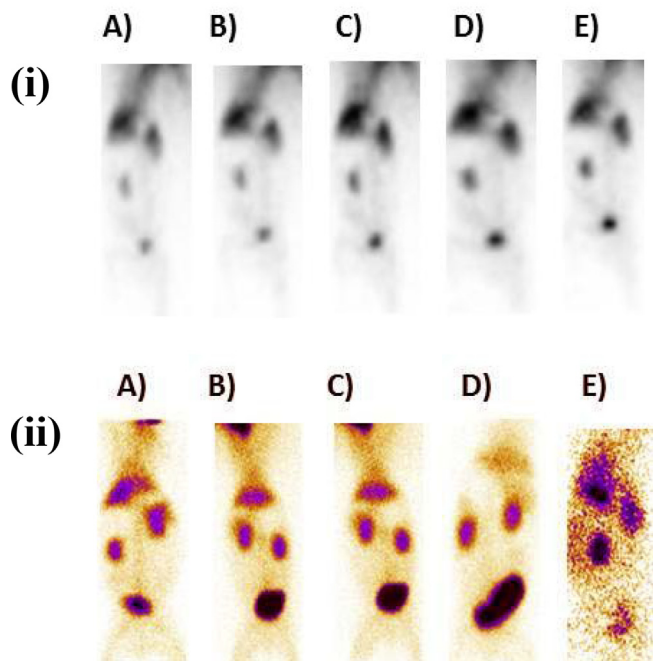


Fig. 12. (i) Scintigraphy profile of ^{99m}Tc -zirconia nanoparticles in dynamic view (anterior mode) in a rabbit model for 1–10 min, after injection. Images at **A)** 1 min, **B)** 3 min, **C)** 5 min, **D)** 7 min, **E)** 10 min and (ii) whole-body static images of rabbit in anterior view indicating the biodistribution of ^{99m}Tc -zirconia nanoparticles at various time points after injection, images at **A)** 15 min **B)** 1 h, **C)** 2 h, **D)** 4 h, and **E)** 24 h.

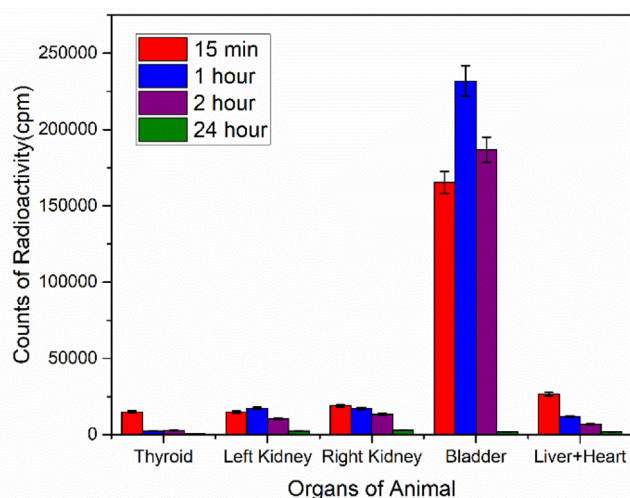


Fig. 13. Uptake of Radio-nanoconjugate in various organs of rabbit at discrete time points.

ples prepared with 1–4 wt% Fe_3O_4 concentration had comparatively low hardness values [Fig. S2 (a–d)]. Whereas, cracks may form as a result of the structural shift from tetragonal to monoclinic (Batool et al., 2020).

Biodegradation test of as synthesized optimized sample, as shown in Fig. 8(a) was measured by means of Eq. (7) (Öchsner and Merkel, 2013).

$$V_s = \frac{S_a}{10} \quad (7)$$

Where V_s and S_a are the volume of SBF (mL) and disc's area (mm^2) respectively. Samples were dipped into a little quantity of SBF before being heated to 36°C , which is the average human body temperature. The disks were washed, and drying was performed at room temperature without any further heat treatment. Using Eq. (8), the possible weight reduction (%) was calculated (Öchsner and Merkel, 2013).

$$\text{Weightloss}(\%) = \frac{W_1 - W_2}{W_1} \times 100 \quad (8)$$

Where w_1 and w_2 are the weight of the compact disc before and after being soaked, respectively. The weight loss data is shown in Fig. 9(a).

Fig. 8(b) demonstrated that the encapsulation efficiency of IOZH nanoparticles was high as compared to the other samples. Optimized samples rapidly encapsulated within first half hour, tailed by gradual encapsulation. After 120 min, the encapsulation efficiency was determined to be $\sim 73\%$ [Fig. 9(b)]. The interaction of hydrogen ions (positively charged and found in curcumin) with iron and oxygen ions (negatively charged) might be the reason of this rapid encapsulation.

Eq. (9) (Gooneh-Farahani et al., 2020) was utilized to test the efficacy of encapsulated drug using stabilized nanoparticles.

$$\text{Encapsulation efficiency}(\%) = ((T_c - S_c) / T_c) * 100 \quad (9)$$

T_c shows total amount of curcumin and S_c shows curcumin present in the supernatant.

Fig. 8(c) shows nanoparticles and ascorbic acid in order to compare the scavenging % of as synthesized samples. To evaluate the absorbance value, UV-visible spectrophotometer was employed. The free radical scavenging capacity of DPPH was examined by using the subsequent Eq. (10) (Lee et al., 2014):

$$\text{Scavenging capability}(\text{SC}\%) = ((A_0 - A_s) / A_0) * 100 \quad (10)$$

The symbols A_0 and A_s reflect the values of DPPH absorption obtained in the absence as well as presence of IOZH nanoparticles tested for antioxidant activity, respectively.

The observed percentage of scavenging inhibition capability with the optimized sample was $\sim 70\%$. This enhanced antioxidant activity is associated with the smaller particles size as well as electron cloud, carried by IOZH nanoparticles. above described findings suggested that these as synthesized IOZH nanoparticles are not only safe to be administrated for imaging purpose but, also, capable of reducing excess amount of ROS.

The effect of nanoparticles on the cell viability of cancer cells is shown in Fig. 8(d). Cells were subjected to varied nanoparticle concentrations to investigate the influence of IOZH nanoparticles on the viability of cancer cells (Gooneh-Farahani et al., 2020). The MTT (3-(4, 5 dimethylthiazol-2-yl)-2, 5diphenyl tetrazolium bromide) test assay was used to measure the percentage viability of the as synthesized IOZH sample. Cells were cultured for a time period of 24 h at a temperature of 37°C prior to exposure of optimized IOZH nanoparticles in this assay. During a time period of 24 h incubation, different IOZH nanoparticle concentrate ions were applied to the well plates at the temperature of 37°C with CO_2 (5%) and air (95%). This procedure was performed in triplicate with untreated (HCT-116) cells acting as a control treatment. Under the same settings, MTT was added to the microplates and incubated for a time period of 4 h. A micro pipit was subsequently utilized to eject the media. Dimethyl sulfoxide (DMSO) was employed to decompose MTT-generated formazan crystals, and the plates were well agitated. At 570 nm, absorbance was measured using a microplate reader. Eq. (11) (Rajapriya et al., 2020) was used to determine the percentage of cell inhibition.

$$\text{Cell inhibition}(\%) = (1 - A_s / A_0) * 100 \quad (11)$$

Here A_s and A_o represents sample and control absorbance, i.e. untreated cancer cells, respectively.

The outcomes of this assay suggested that cell viability is concentration dependent i.e. it decreases as concentration of working solution increases. These health hazard cancerous cells demonstrated around $\sim 23.4\%$ of cell viability after a time period of 24 h after treatment with working solution having 25 $\mu\text{g}/\text{mL}$ concentration. The percentage of cell viability in HCT-116 cells, as shown in Fig. 8 (d) showed that iron oxide stabilized nanoparticles are toxic to malignant cell lines and might be used in cancer therapies.

Gram Stained microbial images [Fig. 10] were observed by making smeared of bacterial culture from extreme edge of inhibition zone for each plates shown in Fig. 9. Fig. 10(b) shows the effect of nanoparticle (having 6 wt% of iron content) treatment. It was observed that sporulating stages were increased as compared to the mature spores and the cells are arranged in the form of pairs. The formation of spores is mainly due to the stress provided. It can be seen that the spores retained some of the stains in this case but originally can be observed in colorless form. In Fig. 10(c, d) it can be observed that increasing concentration of NPs affects gram staining as well as result in early sporulation under stress conditions. The staining color shift from gram positive to gram negative/gram variable can also be observed from Fig. 10. The cell size reduced and chains of bacteria were reduced to single or double cells. The cell size and resolution has also been affected greatly. The staining results in Fig. 10 (f, g) shows the effect of highest concentration of NPs against the *Bacillus subtilis* strain. The cells completely went to the endospore stage and the cell size was reduced. It can be seen that the resolution of bacteria has also been affected and vegetative cells have been reduced and sporulation increased to deal with the stress provided.

To assess an optimum value of pH for doing radiolabeling, the zirconia nanoparticles were labeled with Tc-99 m at various pH (4–7) values. In all experiments, a constant amount of $\text{SnCl}_2 \cdot 2\text{H}_2\text{O}$, e.g., 40 μg , was used to reduce the Tc-99 m metal. The data from these investigations show that at pH 4, the radiolabeling yield was $96 \pm 2\%$ which reduced to $91 \pm 2\%$ at pH 5, dramatically lowered to $87 \pm 2\%$ at pH 6 and further dropped to 81% at pH 7 that was not in acceptable range. So, pH 4 was selected as optimum value for radiolabeling because it produced the highest labeling efficacy [Fig. 11 (a)].

Results presented in Fig. 11(b) indicate that the radiolabeling efficacy (%) by using reducing agent in the range 20–40 μg was 82%, 87% and 96%, respectively. However, the maximum radiolabeling yield, e.g., greater than $95 \pm 2\%$ was observed by using 40 μg of reducing agent.

The radiolabeling yield (%), shown in Fig. 11 (c), was $96 \pm 2\%$ after 30 min of incubation that was equally stable up to 4 h and further decreased to $90 \pm 2\%$ after 24 h.

The data, shown in Fig. 11 (d), clearly indicate that the radiolabeled nanoparticles were stable more than $90 \pm 2\%$ up to 24 h. The effect of amount of ligand, e.g. (zirconia nanoconjugate) on radiolabeling yield (%) was evaluated by varying the amount of the ligand required in radioconjugate formulation. The data indicate that at low value of ligand, e.g. 250 μg , the radiolabeling yield was very low, e.g. $85 \pm 2\%$, which increased to maximum value of $96 \pm 2\%$ at 500 μg of the ligand, and significantly dropped to $70 \pm 1\%$ by further enhancing the amount of ligand to 750 μg . The data are graphically shown in Fig. 11 (e).

Lipophilicity study revealed that the radiolabeled zirconia particles are hydrophilic in nature. Additionally, the nanoparticle-based radio-conjugates bind to a diversity of protein molecules abundant in the plasma, leading to very little drug in the blood.

The amount of free or unbound medicine in the human body might just have significant adverse consequences or pharmacological activity. The recent study showed that $82.3 \pm 1.5\%$ of $^{99\text{m}}\text{Tc}$ -zirconia nanoconjugate displayed binding with proteins in blood, which is much higher than expected for strong binding with proteins.

The scintigraphy results [Figs. 12 and 13] show that the radio-tracer (after injection) is initially taken up by the heart, then by the liver, which is removed slowly, and lastly stored in the bladder, where a gradual increase in activity level is noted with time. That might be because the $^{99\text{m}}\text{Tc}$ -zirconia nanoparticles attach to bladder cells quickly and specifically, indicating the prospect of practical application in the identification of bladder malignancies. Previously Sung et al., (2015), Blasiak et al., (2013) and Büyükkök et al (2019) used nanoparticles for diagnosis and therapy.

As it can be clearly anticipated from the pre-clinical data that the most probable pathway for the excretion of radio-nanoconjugate and its associated metabolites was through the kidney which is considered as the normal excretory route in nuclear medicine procedures so it should be considered as an additional diagnostic feature of the novel nano-tracer under investigation.

5. Conclusions

To fulfil the increased mandate of nanoparticles to be used in biomedical applications, the Fe_3O_4 stabilized zirconia nanostructures were synthesized by using sol–gel route. Iron oxide sol was added to zirconia sol at a concentration of 1–10 wt% (with a 1 wt % interval), and honey was used as a capping agent. The findings of X-ray diffractions revealed a reduction in volume and crystallite size of as synthesized samples when 5 wt- 10 wt% Fe_3O_4 concentrations were added. In the instance of phase pure tetragonal zirconia, reducing the volume of nanoparticles resulted in a better value of hardness and fracture toughness. Tetragonally stabilized samples exhibit dielectric constant values that are suitable for biological applications. High anti-oxidant activity ($\sim 70\%$) as well as highest cell viability against cancerous cell ($\sim 23.4\%$) was observed in optimized sample. Almost 70% of encapsulation efficiency was observed for optimized sample after time period of 120 min. Biodistribution of Sodium Pertechnetate ($\text{Na}^{99\text{m}}\text{TcO}_4$) labelled zirconia nanoparticles showed high uptake by the bladder and negligible uptake in heart and kidney indicating the *in-vivo* stability of labeled conjugates. Results obtained using these characterizations shows that these nanoparticles could be used for future therapeutic as well as drug carrying agents.

Declaration of Competing Interest

The authors declare that they have no known competing financial interests or personal relationships that could have appeared to influence the work reported in this paper.

Acknowledgement

Authors are thankful to Higher Education Commission (HEC), Pakistan, for providing research grant to Centre of Excellence in Solid State Physics. The authors extend their appreciation to Researchers Supporting Project number (RSP2023R165), King Saud University, Riyadh, Saudia Arabia.

Appendix A. Supplementary data

Supplementary data to this article can be found online at <https://doi.org/10.1016/j.arabjc.2023.105267>.

References

- Abd Elmaboud, Y., Mekheimer, K.S., Emam, T.G., 2019. Numerical examination of gold nanoparticles as a drug carrier on peristaltic blood flow through physiological vessels: cancer therapy treatment. *BioNanoScience* 9 (4), 952–965.
- Adeyemi, J.O., Onwudiwe, D.C., Oyediji, A.O., 2022. Biogenic Synthesis of CuO, ZnO, and CuO–ZnO Nanoparticles Using Leaf Extracts of *Dovyalis caffra* and Their Biological Properties. *Molecules* 27 (10), 3206.
- American Society for Testing of Materials 1999. Designation C1327-99 Standard test method for Vickers indentation hardness of advanced ceramics Annual Book of ASTM Standards 15.01. ASTM, Philadelphia.
- Asha, S.B., Muthuraj, D., Kumar, E., Veeraputhiran, V., 2019. Synthesis and Characterization of ZrO₂ Nanoparticles using Microwave Assisted Method and Its Antimicrobial Activity. *Journal of Nanoscience and Technology*, 642–644.
- Avedisian, C.T., Cavicchi, R.E., McEuen, P.L., Zhou, X., 2009. Nanoparticles for cancer treatment: role of heat transfer. *Ann. N. Y. Acad. Sci.* 1161 (1), 62–73.
- Bahari, N., Hashim, N., Abdan, K., Md Akim, A., Maringgal, B., Al-Shdifat, L., 2023. Role of Honey as a Bifunctional Reducing and Capping/Stabilizing Agent: Application for Silver and Zinc Oxide Nanoparticles. *Nanomaterials* 13 (7), 1244.
- Balasooriya, E.R., Jayasinghe, C. D., Jayawardena, U. A., Ruwanthika, R. W. D., Mendis de Silva, R., & Udagama, P. V. (2017). Honey mediated green synthesis of nanoparticles: new era of safe nanotechnology. *Journal of Nanomaterials*, 2017.
- Balaji, S., Mandal, B.K., Ranjan, S., Dasgupta, N., Chidambaram, R., 2017. Nano-zirconia—evaluation of its antioxidant and anticancer activity. *Journal of Photochemistry and Photobiology B: Biology* 170, 125–133.
- Bashir, M., Riaz, S., Naseem, S., 2015. Fe₃O₄ stabilized zirconia: structural, mechanical and optical properties. *J. Sol-Gel Sci. Technol.* 74 (2), 281–289.
- Batool, T., Bukhari, B.S., Riaz, S., Batoo, K.M., Raslan, E.H., Hadi, M., 2020. Microwave assisted sol-gel synthesis of bioactive zirconia nanoparticles—Correlation of strength and structure. *J. Mech. Behav. Biomed. Mater.* 112, 104012.
- Blasiak, B., van Veggel, F.C., & Tomanek, B. (2013). Applications of nanoparticles for MRI cancer diagnosis and therapy. *Journal of Nanomaterials*, 2013, 12–12.
- Bokov, D., Turki Jalil, A., Chupradit, S., Suksatan, W., Javed Ansari, M., Shewael, I.H., Valiev, G.H., Kianfar, E., 2021. Nanomaterial by sol-gel method: synthesis and application. *Adv. Mater. Sci. Eng.* 2021, 1–21.
- Bukhari, S.B., Imran, M., Bashir, M., Riaz, S., Naseem, S., 2018. Room temperature stabilized TiO₂ doped ZrO₂ thin films for teeth coatings—A sol-gel approach. *J. Alloy. Compd.* 767, 1238–1252.
- Büyükkök, O., Ucar, E., İçhedef, Ç., Çetin, O., Teksöz, S., 2019. Bioevaluation of 99mTc (I) carbonyl-radiolabeled amino acid coated magnetic nanoparticles in vivo. *Materials Chemistry and Physics* 235, 121751.
- Cadafalch Gazquez, G., Chen, H., Veldhuis, S.A., Solmaz, A., Mota, C., Boukamp, B.A., Moroni, L., 2016. Flexible yttrium-stabilized zirconia nanofibers offer bioactive cues for osteogenic differentiation of human mesenchymal stromal cells. *ACS Nano* 10 (6), 5789–5799.
- Cai, K., Bossert, J., Jandt, K.D., 2006. Does the nanometre scale topography of titanium influence protein adsorption and cell proliferation? *Colloids Surf. B Biointerfaces* 49 (2), 136–144.
- Cao, Z., An, S., Song, X., 2022. Effect of thermal treatment at high temperature on phase stability and transformation of Yb₂O₃ and Y₂O₃ co-doped ZrO₂ ceramics. *Sci. Rep.* 12 (1), 9955.
- Chakravarty, R., Shukla, R., Ram, R., Tyagi, A.K., Dash, A., Venkatesh, M., 2010. Practicality of tetragonal nano-zirconia as a prospective sorbent in the preparation of 99 Mo/99m Tc generator for biomedical applications. *Chromatographia* 72, 875–884.
- Cheng, K., Weng, W., Wang, H., Zhang, S., 2005. In vitro behavior of osteoblast-like cells on fluoridated hydroxyapatite coatings. *Biomaterials* 26 (32), 6288–6295.
- Cong, Y., Li, B., Yue, S., Fan, D., Wang, X.J., 2009. Effect of oxygen vacancy on phase transition and photoluminescence properties of nanocrystalline zirconia synthesized by the one-pot reaction. *J. Phys. Chem. C* 113 (31), 13974–13978.
- Cullity, B.D., 1956. *Elements of X-Ray Diffraction*. Addison-Wesley, New York, NY, USA.
- Das, D., Nath, B.C., Phukon, P., Dolui, S.K., 2013. Synthesis of ZnO nanoparticles and evaluation of antioxidant and cytotoxic activity. *Colloids Surf. B Biointerfaces* 111, 556–560.
- Dasgupta, S., Auth, T., Gompper, G., 2017. Nano-and microparticles at fluid and biological interfaces. *J. Phys. Condens. Matter* 29 (37), 373003.
- Davar, F., Hassankhani, A., Loghman-Estarki, M.R., 2013. Controllable synthesis of metastable tetragonal zirconia nanocrystals using citric acid assisted sol-gel method. *Ceram. Int.* 39 (3), 2933–2941.
- El-Kased, R.F., Amer, R.I., Attia, D., Elmazar, M.M., 2017. Honey-based hydrogel: in vitro and comparative in vivo evaluation for burn wound healing. *Sci. Rep.* 7 (1), 1–11.
- Fang, D., Luo, Z., Liu, S., Zeng, T., Liu, L., Xu, J., Xu, W., 2013. Photoluminescence properties and photocatalytic activities of zirconia nanotube arrays fabricated by anodization. *Opt. Mater.* 35 (7), 1461–1466.
- Farahani, S.G., Naghib, S.M., Naimi-Jamal, M.R., 2020. A Novel and Inexpensive Method Based on Modified Ionic Gelation for pH-responsive Controlled Drug Release of Homogeneously Distributed Chitosan Nanoparticles with a High Encapsulation Efficiency. *Fibers and Polymers* 21 (9), 1917–1926.
- Gabriel, S., Lau, R.W., Gabriel, C., 1996. The dielectric properties of biological tissues: II. Measurements in the frequency range 10 Hz to 20 GHz. *Phys. Med. Biol.* 41 (11), 2251.
- Garvie, R. C., Hannink, R. H., & Pascoe, R. T. 1975. Ceramic Steel, 258 (703). Nature, London.
- Gooneh-Farahani, S., Naghib, S.M., Naimi-Jamal, M.R., 2020. A novel and inexpensive method based on modified ionic gelation for pH-responsive controlled drug release of homogeneously distributed chitosan nanoparticles with a high encapsulation efficiency. *Fibers Polym.* 21, 1917–1926.
- Gottenbos, B., Grijpma, D.W., van der Mei, H.C., Feijen, J., Busscher, H.J., 2001. Antimicrobial effects of positively charged surfaces on adhering Gram-positive and Gram-negative bacteria. *J. Antimicrob. Chemother.* 48 (1), 7–13.
- Guo, F., Xiao, P., 2012. Effect of Fe₂O₃ doping on sintering of yttria-stabilized zirconia. *J. Eur. Ceram. Soc.* 32 (16), 4157–4164.
- Han, J., Malek, O., Vleugels, J., Braem, A., Castagne, S., 2022. Ultrashort pulsed laser ablation of zirconia-alumina composites for implant applications. *J. Mater. Process. Technol.* 299, 117335.
- Harianawala, H., Kheur, M., Kheur, S., Sethi, T., Bal, A., Burhanpurwala, M., Sayed, F., 2016. Biocompatibility of zirconia. *Journal of Advanced Medical and Dental Sciences Research* 4 (3), 35.
- Hbaieb, K., 2012. Reducing sintering temperature of yttria stabilized zirconia through addition of lithium nitrate and alumina. *Ceram. Int.* 38 (5), 4159–4164.
- Heshmatpour, F., Aghakhanpour, R.B., 2011. Synthesis and characterization of nanocrystalline zirconia powder by simple sol-gel method with glucose and fructose as organic additives. *Powder Technol.* 205 (1–3), 193–200.
- Hiremath, P.G., Rajashekara, S., Binnal, P., & Theodore, T. 2021. Chapter 9—Fluoride Contamination in Underground Water and Its Treatment. *Management of Contaminants of Emerging Concern (CEC) in Environment*; Singh, P., Hussain, CM, Rajkhowa, S., Eds, 249–280.
- Holz, L., Macias, J., Vitorino, N., Fernandes, A.J.S., Costa, F.M., Almeida, M.M., 2018. Effect of Fe₂O₃ doping on colour and mechanical properties of Y-TZP ceramics. *Ceram. Int.* 44 (15), 17962–17971.
- Imran, M., Riaz, S., Sanaullah, I., Khan, U., Sabri, A.N., Naseem, S., 2019. Microwave assisted synthesis and antimicrobial activity of Fe₃O₄-doped ZrO₂ nanoparticles. *Ceram. Int.* 45 (8), 10106–10113.
- Imran, M., Riaz, S., Batool, T., Qamar, A., Khan, I.U., Zahoor, R., Naseem, S., 2021. Biodistribution of iron-oxide-stabilized 99m Tc-ZrO₂ nanoparticles in rabbit using honey as a capping agent—microwave-assisted sol-gel approach. *J. Sol-Gel Sci. Technol.* 98, 95–112.
- Jain, T.K., Reddy, M.K., Morales, M.A., Leslie-Pelecky, D.L., Labhasetwar, V., 2008. Biodistribution, clearance, and biocompatibility of iron oxide magnetic nanoparticles in rats. *Mol. Pharm.* 5 (2), 316–327.
- Jameel, M.S., Aziz, A.A., Dheyab, M.A., 2020. Comparative analysis of platinum nanoparticles synthesized using sonochemical-assisted and conventional green methods. *Nano-Structures & Nano-Objects* 23, 100484.
- Janes, K.A., Fresneau, M.P., Marazuela, A., Fabra, A., Alonso, M.J. 2001. Chitosan nanoparticles as delivery systems for doxorubicin. *J. Control Release.* 15;73(2–3), 255–67.
- Jha, A.K., 2013. Electrical characterization of zirconium substituted barium titanate using complex impedance spectroscopy. *Bull. Mater. Sci.* 36 (1), 135–141.
- Ji, Z., Brace, C.L., 2011. Expanded modeling of temperature-dependent dielectric properties for microwave thermal ablation. *Phys. Med. Biol.* 56 (16), 5249.
- Jodłowski, P.J., Chlebda, D.K., Jędrzejczyk, R.J., Dziedzicka, A., Kuterasiński, Ł., Sitarz, M., 2018. Characterisation of well-adhered ZrO₂ layers produced on structured reactors using the sonochemical sol-gel method. *Appl. Surf. Sci.* 427, 563–574.
- Kanth Kadiyala, N., Mandal, B.K., Kumar Reddy, L.V., Barnes, C.H., Valladares, D.L.S., L., & Sen, D., 2023. Efficient One-Pot Solvothermal Synthesis and Characterization of Zirconia Nanoparticle-Decorated Reduced Graphene Oxide Nanocomposites: Evaluation of Their Enhanced Anticancer Activity toward Human Cancer Cell Lines. *ACS Omega* 8 (2), 2406–2420.
- Kao, C.T., Tuan, W.H., Liu, C.Y., Chen, S.C., 2018. Effect of iron oxide coloring agent on the sintering behavior of dental yttria-stabilized zirconia. *Ceram. Int.* 44 (5), 4689–4693.
- Kelly, J.R., Denry, I., 2008. Stabilized zirconia as a structural ceramic: an overview. *Dent. Mater.* 24 (3), 289–298.
- Khalili, S., Chenari, H.M., 2020. Successful electrospinning fabrication of ZrO₂ nanofibers: A detailed physical-chemical characterization study. *J. Alloy. Compd.* 828, 154414.
- Khan, H.N., Imran, M., Sanaullah, I., Khan, I.U., Sabri, A.N., Naseem, S., Riaz, S., 2023. In vivo biodistribution, antioxidant and hemolysis tendency of superparamagnetic iron oxide nanoparticles—Potential anticancer agents. *Arab. J. Chem.* 16 (4), 104602.
- Lee, S.Y., Mediani, A., Ashikin, A.N., Azliana, A.B.S., Abas, F., 2014. Antioxidant and [alpha]-glucosidase inhibitory activities of the leaf and stem of selected traditional medicinal plants. *Int. Food Res. J.* 21 (1), 379.
- Li, K., Chen, J., Peng, J., Koppala, S., Omran, M., Chen, G., 2020. One-step preparation of CaO-doped partially stabilized zirconia from fused zirconia. *Ceram. Int.* 46 (5), 6484–6490.
- Lin, W.C., Chuang, C.C., Wang, P.T., Tang, C.M., 2018. A comparative study on the direct and pulsed current electrodeposition of cobalt-substituted hydroxyapatite for magnetic resonance imaging application. *Materials* 12 (1), 116.
- Liu, H., Dandy, D.S., Liu, H., Dandy, D.S., 1995. Effects of Surface Conditions on Diamond Nucleation. *Diam. Chem. Vap. Depos.* 92–130.
- Lopez, D.E., Suwannakarn, K., Bruce, D.A., Goodwin Jr, J.G., 2007. Esterification and transesterification on tungstated zirconia: Effect of calcination temperature. *J. Catal.* 247 (1), 43–50.

- Lu, N., He, G., Yang, Z., Yang, X., Li, Y., Li, J., 2022. Fabrication and reaction mechanism of MgO-stabilized ZrO₂ powders by combustion synthesis. *Ceram. Int.* 48 (5), 7261–7264.
- Lübber, A.S., Alexiou, C., Bergemann, C., 2001. Clinical applications of magnetic drug targeting. *J. Surg. Res.* 95 (2), 200–206.
- Macdonald, J.R., Barsoukov, E., 2005. Impedance spectroscopy: theory, experiment, and applications. *History* 1 (8), 1–583.
- Manjunatha, K.B., Bhat, R.S., Shashidhara, A., Kumar, H.A., Nagashree, S., 2021. Antimicrobial and nonlinear optical studies of copper oxide nanoparticles. *J. Electron. Mater.* 50, 3415–3421.
- Marsh, B.D., 1998. On the interpretation of crystal size distributions in magmatic systems. *J. Petrol.* 39 (4), 553–599.
- Miller, J.S., 2011. Magnetically ordered molecule-based materials. *Chem. Soc. Rev.* 40 (6), 3266–3296.
- Miller, J.S., Epstein, A.J., 1994. Organic and organometallic molecular magnetic materials—designer magnets. *Angew. Chem. Int. Ed. Eng.* 33 (4), 385–415.
- Mittal, A., Roy, I., Gandhi, S., 2022. Magnetic nanoparticles: An overview for biomedical applications. *Magnetochemistry* 8 (9), 107.
- Mohanty, C., Sahoo, S.K., 2010. The in vitro stability and in vivo pharmacokinetics of curcumin prepared as an aqueous nanoparticulate formulation. *Biomaterials* 31, 6597–6611.
- Muthulakshmi, N., Kathirvel, A., Subramanian, R., Senthil, M., 2023. Biofabrication of zirconia nanoparticles: synthesis spectral characterization and biological activity evaluation against pathogenic bacteria. *Biointerface Res Appl Chem* 13, 190.
- Natalia, V., Rahmawati, F., Purwanto, A., 2018. Crystal structure analysis of lithium zirconate prepared from local sand at a various ratio of Li₂CO₃ to ZrO₂. *Space* 12, c1.
- Niihara, K., Morena, R., Hasselman, D.P.H., 1982. Evaluation of K_{1c} of brittle solids by the indentation method with low crack-to-indent ratios. *J. Mater. Sci. Lett.* 1 (1), 13–16.
- Nishakavya, S., Girigoswami, A., Gopikrishna, A., Deepa, R., Divya, A., Ajith, S., Girigoswami, K., 2022. Size attenuated copper doped zirconia nanoparticles enhances in vitro antimicrobial properties. *Appl. Biochem. Biotechnol.* 194 (8), 3435–3452.
- Öchsner, A., Merkel, M., 2013. Bending Element. In *One-Dimensional Finite Elements*. Springer, Berlin, Heidelberg, pp. 57–110.
- Ordóñez, F., Chejne, F., Pabón, E., Cacia, K., 2020. Synthesis of ZrO₂ nanoparticles and effect of surfactant on dispersion and stability. *Ceram. Int.* 46 (8), 11970–11977.
- Pattnaik, S., Nethala, S., Tripathi, A., Saravanan, S., Moorthi, A., Selvamurugan, N., 2011. Chitosan scaffolds containing silicon dioxide and zirconia nano particles for bone tissue engineering. *International journal of biological macromolecules* 49 (5), 1167–1172.
- Peer, D., Karp, J.M., Hong, S., Farokhzad, O.C., Margalit, R., Langer, R., 2020. Nanocarriers as an emerging platform for cancer therapy. *Nano-Enabled Medical Applications*, 61–91.
- Peng, E., Wei, X., Garbe, U., Yu, D., Edouard, B., Liu, A., Ding, J., 2018. Robocasting of dense yttria-stabilized zirconia structures. *J. Mater. Sci.* 53, 247–273.
- Philip, D., 2009. Honey mediated green synthesis of gold nanoparticles. *Spectrochim. Acta A Mol. Biomol. Spectrosc.* 73 (4), 650–653.
- Pijera, M.S.O., Viltres, H., Kozempel, J., Sakmár, M., Vlk, M., İlem-Özdemir, D., Santos-Oliveira, R., 2022. Radiolabeled nanomaterials for biomedical applications: radiopharmacy in the era of nanotechnology. *EJNMMI Radiopharm Chem.* 7 (1), 8.
- Quintard, P.E., Barbéris, P., Mirgorodsky, A.P., Merle-Méjean, T., 2002. Comparative lattice-dynamical study of the Raman spectra of monoclinic and tetragonal phases of zirconia and hafnia. *J. Am. Ceram. Soc.* 85 (7), 1745–1749.
- Rahman, A.M., Yusuf, S.W., Ewer, M.S., 2007. Anthracycline-induced cardiotoxicity and the cardiac-sparing effect of liposomal formulation. *Int. J. Nanomed.* 2 (4), 567.
- Rajapriya, M., Sharmili, S.A., Baskar, R., Balaji, R., Alharbi, N.S., Kadaikunnan, S., Vaseeharan, B., 2020. Synthesis and characterization of zinc oxide nanoparticles using *Cynara scolymus* leaves: enhanced hemolytic, antimicrobial, antiproliferative, and photocatalytic activity. *J. Clust. Sci.* 31 (4), 791–801.
- Renger, C., Kuschel, P., Kristoffersson, A., Clauss, B., Oppermann, W., Sigmund, W., 2004. Colloid probe investigation of the stabilization mechanism in aqueous 1,2-propanediol nano-zirconia dispersions. *PCCP* 6 (7), 1467–1474.
- Sahoo, S., Chakraborti, C.K., Mishra, S.C., 2011. Qualitative analysis of controlled release ciprofloxacin/carbopol 934 mucoadhesive suspension. *J. Adv. Pharm. Technol. Res.* 2 (3), 195.
- Sajjadi, S., 2007. Nanoparticle formation by monomer-starved semibatch emulsion polymerization. *Langmuir* 23 (3), 1018–1024.
- Sajjadi, S., Brooks, B.W., 2000. Unseeded semibatch emulsion polymerization of butyl acrylate: bimodal particle size distribution. *J. Polym. Sci. A Polym. Chem.* 38 (3), 528–545.
- Sanaullah, I., Bukhari, B.S., Batool, T., Riaz, S., Khan, H.N., Sabri, A.N., Naseem, S., 2020. Antibacterial performance of glucose-fructose added MW based zirconia coatings—Possible treatment for bone infection. *J. Mech. Behav. Biomed. Mater.* 104, 103621.
- Sanaullah, I., Bashir, M., Batool, T., Riaz, S., Ali, D., Sabri, A.N., Naseem, S., 2021. Tangerine mediated synthesis of zirconia as potential protective dental coatings. *Mater. Sci. Eng. C* 120, 111653.
- Sanaullah, I., Imran, M., Riaz, S., Amin, T., Khan, I.U., Zahoor, R., Naseem, S., 2021. Microwave assisted synthesis of Fe₃O₄ stabilized ZrO₂ nanoparticles—Free radical scavenging, radiolabeling and biodistribution in rabbits. *Life Sci.* 271, 119070.
- SanaUllah, I., Khan, H.N., Saleha, M., Imran, M., Raza, M.A., Sajjad, A., Riaz, S., 2022. Free radical scavenging and antimicrobial activities of MW assisted sol-gel synthesized honey mediated zirconia. *J. Sol-Gel Sci. Technol.* 103 (2), 457–475.
- Sanghani, A., Nag, O.K., Field, L.D., Breger, J.C., Delehanty, J.B., 2017. Multifunctional nanoparticle composites: progress in the use of soft and hard nanoparticles for drug delivery and imaging. *Wiley Interdiscip. Rev. Nanomed. Nanobiotechnol.* 9 (6), e1466.
- Sengupta, P., Bhattacharje, A., Maiti, H.S., 2019. Zirconia: A unique multifunctional ceramic material 72, 1981–1998.
- Serpen, A., Capuano, E., Fogliano, V., Gökmen, V., 2007. A New Procedure To Measure the Antioxidant Activity of Insoluble Food Components. *J. Agric. Food Chem.* 55, 7676–7681.
- Shin, G.-J., Jeong, S.-Y., Lee, J.-W., 2017. Evaluation of antioxidant activity of the residues generated from ethanol concentration of lignocellulosic biomass using pervaporation. *Journal of Industrial and Engineering Chemistry* 52, 51–58.
- Singh, M., Yadav, B.C., Ranjan, A., Kaur, M., Gupta, S.K., 2017. Synthesis and characterization of perovskite barium titanate thin film and its application as LPG sensor. *Sens. Actuators B* 241, 1170–1178.
- Smeacetto, F., Salvo, M., Ajitdoss, L.C., Perero, S., Moskalewicz, T., Boldrini, S., Doubova, L., Ferraris, M., 2010. Yttria-stabilized zirconia thin film electrolyte produced by RF sputtering for solid oxide fuel cell applications. *Mater. Lett.* 64 (22), 2450–2453.
- Sundell, P.G., Björketun, M.E., Wahnström, G., 2006. Thermodynamics of doping and vacancy formation in BaZrO₃ perovskite oxide from density functional calculations. *Phys. Rev. B* 73 (10), 104112.
- Sung Lee, J., Myung Cha, J., Young Yoon, H., Lee, J.K., Keun Kim, Y., 2015. Magnetic multi-granule nanoclusters: A model system that exhibits universal size effect of magnetic coercivity. *Scientific reports* 5 (1), 12135.
- Tyagi, B., Sidhpuria, K., Shaik, B., Jasra, R.V., 2006. Synthesis and characterization of nanocrystalline mesoporous zirconia using supercritical drying. *J. Nanosci. Nanotechnol.* 6 (6), 1584–1593.
- Venu, R., Ramulu, T.S., Anandakumar, S., Rani, V.S., Kim, C.G., 2011. Bio-directed synthesis of platinum nanoparticles using aqueous honey solutions and their catalytic applications. *Colloids Surf A Physicochem Eng Asp* 384 (1–3), 733–738.
- Xia, C., Hu, C., Tian, Y., Chen, P., Wan, B., Xu, J., 2011. Room-temperature ferromagnetic properties of Fe-doped ZnO rod arrays. *Solid State Sci.* 13 (2), 388–393.
- Xu, X., Guo, G., Fan, Y., 2010. Fabrication and characterization of dense zirconia and zirconia-silica ceramic nanofibers. *J. Nanosci. Nanotechnol.* 10 (9), 5672–5679.
- Yentekakis, I. V., & Chu, W., 2020. Advances in Heterocatalysis by Nanomaterials.
- Yuan, Y., Wu, Y., Suganthi, N., Shanmugam, S., Brindhadevi, K., Sabour, A., Shanmuganathan, R., 2022. Biosynthesis of zirconium nanoparticles (ZrO₂ NPs) by *Phyllanthus niruri* extract: Characterization and its photocatalytic dye degradation activity. *Food Chem. Toxicol.* 168, 113340.
- Zhao, Y., Tang, Y., Guo, Y., Bao, X., 2010. Studies of electrospinning process of zirconia nanofibers. *Fibers Polym.* 11 (8), 1119–1122.
- Zhukovskaya, A.E., Strakhov, V.I., 1980. Effect of iron oxide on the phase composition of zirconia refractories. *Refractories* 21 (1–2), 48–52.